Author/s:
Bagherjeri, FA;Vonci, M;Nagul, EA;Ritchie, C;Gable, RW;Taylor, MB;Bryant, G;Guo, SX;Zhang, J;Aparicio, PA;López, X;Poblet, JM;Boskovic, C

Title:
Mixed-Metal Hybrid Polyoxometalates with Amino Acid Ligands: Electronic Versatility and Solution Properties

Date:
2016-12-05

Citation:
Bagherjeri, F. A., Vonci, M., Nagul, E. A., Ritchie, C., Gable, R. W., Taylor, M. B., Bryant, G., Guo, S. X., Zhang, J., Aparicio, P. A., López, X., Poblet, J. M. & Boskovic, C. (2016). Mixed-Metal Hybrid Polyoxometalates with Amino Acid Ligands: Electronic Versatility and Solution Properties. Inorganic Chemistry, 55 (23), pp.12329-12347. https://doi.org/10.1021/acs.inorgchem.6b02218.

Mixed-metal hybrid polyoxometalates with amino acid ligands: electronic versatility and solution properties

Fateme Akhlaghi Bagherjeri,[†] Michele Vonci,[†] Edward A. Nagul, [†] Chris Ritchie,[†] Robert W. Gable,[†] Matthew B. Taylor,[‡] Gary Bryant,[‡] Si-Xuan Guo,[§] Jie Zhang, [§] Pablo A. Aparicio,[⊥] Xavier López,[⊥] Josep M. Poblet[⊥] and Colette Boskovic[,†]*

School of Chemistry, University of Melbourne, Victoria, 3010, Australia; School of Science, RMIT University, Melbourne, Victoria, 3001, Australia; School of Chemistry, Monash University, Clayton, Victoria, 3800, Australia; Department of Physical and Inorganic Chemistry, Universitat Rovira i Virgili, Marcel·lí Domingo 1, 43007 Tarragona, Spain.

c.boskovic@unimelb.edu.au

RECEIVED DATE (to be automatically inserted after your manuscript is accepted if required according to the journal that you are submitting your paper to)

[†] University of Melbourne.

[‡] Monash University

[§] RMIT University.

[⊥] Universitat Rovira i Virgili.

Abstract

Eight new members of a family of mixed-metal (Mo,W) polyoxometalates (POMs) with amino acid ligands have been synthesized and investigated in the solid state and solution using multiple physical techniques. While the parent POM structural framework is conserved, the different analogs vary in nuclearity of the central metal-oxo core, overall redox-state, metal composition, and identity of the zwitterionic α-amino acid ligand. Structural investigations reveal site-selective substitution of Mo for W, with a strong preference for Mo to occupy the central metal-oxo core. This core structural unit is a closed tetrametallic loop in the blue reduced species and an open trimetallic loop in the colorless oxidized analogs. Density functional theory calculations indicate the core as the favored site of reduction and reveal that the LUMO is much lower in energy for a tetra- versus tri-metallic core. The reduced species are diamagnetic, each with a pair of strongly antiferromagnetically coupled Mo^{V} centers in the tetrametallic core, while in the oxidized complexes all Mo is hexavalent. Solution small angle X-ray scattering and circular dichroism (CD) studies indicate that the hybrid POM is stable in aqueous solution on a timescale of days within defined concentration and pH ranges, with stability enhanced by the presence of excess amino acid. The CD experiments also reveal that the amino acid ligands readily exchange with other α-amino acids, but not with water or DMSO, and it is possible to isolate the products of amino acid exchange. Cyclic voltammograms of the reduced species exhibit an irreversible oxidation process at relatively low potential, but an equivalent reductive process is not evident for the oxidized analogs. Despite their overall structural similarity, the oxidized and 2e-reduced hybrid POMs are not interconvertible because of the respective open versus closed loop arrangement in the central metal-oxo cores.

Introduction

For over 100 years, the qualitative and quantitative colorimetric analysis of phosphates, arsenates and similar species has been based on the characteristic "molybdenum blue" color of some reduced polyoxometalates (POMs).[1] Underlying these applications, as well as applications in oxidation catalysis,[2] is the extensive redox chemistry displayed by many of these molecular analogs of metal oxides.[3] Their ability to reversibly accept multiple electrons also confers on POMs a capacity to act as multi-electron reservoirs or transfer agents. Promise for the development of novel electronic materials or water oxidation catalysts for green energy production is thus evident for hybrid compounds that result from covalently attaching redox-active POMs to other moieties with electronic or catalytic activity.[4 5] Polyoxometalate redox chemistry is correlated with photoactivity involving photoreduction of the POM in the presence of organic electron donors,[6,7] or by water at an interface.[8] Reduced POMs can act as chemical reductants,[9] including photoreduced POMs acting as catalysts for water reduction or the formation of precious metal nanoparticles.[10-13] In some cases other metal complexes are required as photosensitizers. The facility of reduction of a particular POM depends on factors including the charge to nuclearity ratio and therefore the nature of the heteroatoms.[14-17] Polyoxomolybdates are more readily reduced than are isostructural polyoxotungstates and Mo atoms are preferentially reduced in mixed metal Mo/W POMs.[18] Notable reduced POMs are the mixed-valence molybdenum blue Mo^{V}/Mo^{VI} "giant wheels" based on $\{Mo_{154}\}$ units,[19- 21] which are obtained by partial reduction of Mo^{VI} solutions at pH < 3. Molybdenum blues are reduced by an even number of electrons with the strongly antiferromagnetically coupled reducing electrons delocalized in pairs over well-defined parts of the POM, resulting in diamagnetism.[22-26] For instance the $\{Mo_{154}\}$ wheel has 28 Mo^{V} centers. While the giant MO wheels and other mixed-valence polyoxomolybdates are often air-stable, the "heteropoly blue" reduced forms of polyoxotungstates are typically air-sensitive.

Tuning the redox, catalytic and other properties of POMs can be achieved by varying the POM composition through several means, including the incorporation of other metal centers, organic ligands

or metal-ligand complexes.[27-35] However, characterization of the resulting species can be challenging, particularly in the case of mixed-valence, mixed-metal compounds, with the application of multiple complementary physical techniques sometimes necessary, even to simply determine the compound formulation. In the case of mixed-metal species, determination of the number and structural positions of the different metal centers can often be achieved through single crystal X-ray diffraction, complemented by elemental analysis. For mixed-valence species, the questions that arise concern firstly the number of reducing electrons and secondly the location and degree of delocalization of these electrons. Crystallography can give insights into the valence of the metal centers, as can EPR and X-ray photoelectron spectroscopy (XPS), while magnetometry can indicate the number of unpaired electrons. In solution, redox titrations, electrochemistry and UV-visible spectroelectrochemistry are most useful for determining the exact degree of reduction. Computational chemistry has also become increasingly accurate and affordable in terms of computation time and the insights provided are invaluable for elucidating the electronic structure of POMs and hybrid POMs.[14,15]

Solution speciation studies have established that POMs interconvert in solution, depending especially on pH and POM concentration.[3] Thus before conclusions can be drawn from chemical or physical properties observed in solution, it is essential to ascertain the identity and stability of the complex in solution, which will also depend on factors such as overall ionic strength, organic solvent and presence of other species. Multinuclear ^{51}V and ^{183}W NMR has been used extensively in this regard, especially for high symmetry polyoxovanadates or polyoxotungstates. [36,37] Mass spectrometry can indicate the composition of the POM in the gas phase and by implication in the solution that was injected into the spectrometer.[38] A technique for investigating the solution structure or solution stability of POMs that has become more prevalent recently is Small Angle X-ray Scattering (SAXS), which can give information about the size and shape of discrete POMs, assemblies of POMs or POM-containing ion pairs or clusters in solution. [37,39-44] Polyoxometalates as small as $[Nb_6O_{19}]^{8-}$ have been characterized by SAXS.[45] Also relevant to this work is the issue of chirality, as POMs can be dissymmetric and thus

intrinsically chiral or chirality can be induced in nominally achiral POMs through covalent binding or electrostatic association of chiral organic moieties.[46-54]

We recently communicated the first two members of a new family of mixed-metal hybrid polyoxometalates with amino acid ligands (Figure 1) of general formula $[As_4(M_4)Mo^{VI}_xW^{VI}_{44-x}Y_4O_{160}(AA)_y(H_2O)_z]^{n-}$ (M = a combination of Mo, W and Y; AA = α-amino acid, x = 0-3, y = 8 or 9).[55] Using *para*-methylbenzylammonium (p-$MeBzNH_3^+$) cations and glycine (Gly) or enantiopure L- or D-norleucine (L-Nle or D-Nle) amino acid ligands (Chart 1), we were able to access structural analogs formulated as $(p\text{-}MeBzNH_3)_6K_2(GlyH)[As_4(YW^{VI}_3)W^{VI}_{44}Y_4O_{159}(Gly)_8(H_2O)_{14}]\cdot 47H_2O$ (**1**) and enantiomorphs $(p\text{-}MeBzNH_3)_{15}(NleH)_3[As_4(Mo^V_2Mo^{VI}_2)W^{VI}_{44}Y_4O_{160}(Nle)_9(H_2O)_{11}]$ $[As_4(Mo^{VI}_2W^{VI}_2)W^{VI}_{44}Y_4O_{160}(Nle)_9(H_2O)_{11}]$ (generically designated **2**: L-Nle, **2a**; D-Nle, **2b**), which together illustrate the structural versatility of this family of compounds. The common yttrium-polyoxotungstate framework of **1** and **2** is reminiscent of long known $[As_4W_{40}O_{140}]^{28-}$ and its lanthanoid derivatives, as well as the more recently reported $[Ln_6(H_2O)_{22}\{As_4W_{44}(OH)_2(proline)_2O_{151}\}]^{10-}$.[56 57 58 59] The zwitterionic amino acid ligands of **1** and **2** bridge the metal centers via carboxylate groups, with the protonated amine groups involved in intramolecular hydrogen bonding to the POM. This framework supports an inner oxo-bridged tetrametallic $\{M_4\}$ "core" (M = Mo, W or Y) and density functional theory (DFT) calculations revealed that the first two reducing electrons are always delocalized on this $\{M_4\}$ core and strongly antiferromagnetically coupled. The resulting diamagnetism was confirmed by magnetic susceptibility and EPR measurements. Diamagnetic compound **2** is thus comprised of an equal mixture of fully oxidized and 2e-reduced POMs. The structural versatility that is evident from **1** and **2** includes (i) preferential metal substitution of Mo for W in the $\{M_4\}$ core, (ii) site-selective reduction of the $\{M_4\}$ core, (iii) the ability to access chiral analogs using chiral amino acid ligands and (iv) the accessibility of different crystal-packing motifs and solubility properties through varying the ligand-cation combination. Although **1** is essentially insoluble, SAXS, electrospray ionization mass spectrometry (ESI-MS), electronic absorption and CD spectroscopy and electrochemical studies of **2** established structural retention of the POM backbone in DMSO and/or Nle buffer (pH = 2.2) on a

timescale of at least a day, although the presence or absence of amino acid ligand exchange was not determined conclusively. Compound **2** is obtained following photoreduction by UV light and is essentially an equal mixture of oxidized and 2e-reduced analogs. To fully elucidate the properties of this family of hybrid POMs, our aims with the present work were three-fold: (i) to obtain a fully 2e-reduced $\{Mo^{V}_{2}\}$-containing analog of **2**, rather than a mixture of complexes with different degrees of reduction, (ii) to achieve complete Mo substitution of the four metal sites in the central tetrametallic core, and (iii) to elucidate the nature of amino acid ligand exchange in solution.

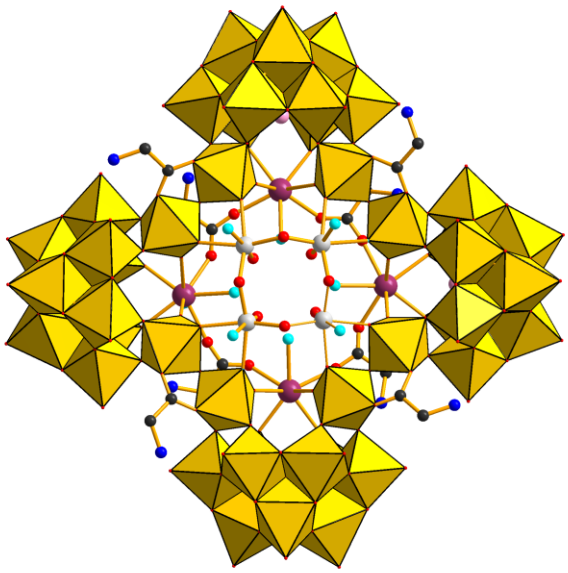

Figure 1. Structural representation of idealized hybrid polyoxometalate $[As_4(M^{VI}_4)W^{VI}_{44}Y_4O_{160}(Gly)_8(H_2O)_{12}]^{8-}$ (M = Mo, W). Color code: WO_6 octahedra, yellow; Y, violet; disordered Mo/W, grey; As, pale blue; C, black; N, dark blue; O, red; aqua ligands, cyan.

Chart 1

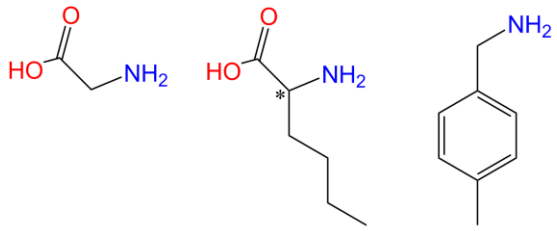

Gly Nle *p*-MeBzNH$_2$

Experimental Section

Synthesis. All manipulations were performed under aerobic conditions, using materials as received. Precursor $K_{14}[As_2W_{19}O_{67}(H_2O)]$ was prepared as described previously.[60]

(*p*-MeBzNH$_3$)$_7$(L-NleH)$_5$[As$_4$(Mo$^{VI}_3$)Mo$^{VI}_{2.5}$W$^{VI}_{41.5}$Y$_4$O$_{159}$(L-Nle)$_8$(H$_2$O)$_{11}$]·20H$_2$O (3). Solid $K_{14}[As_2W_{19}O_{67}(H_2O)]$ (0.5263 g, 0.1000 mmol) was dissolved in 0.2 M L-norleucine solution (15 ml, 3.0 mmol) at pH 2.2, with this pH maintained during the dissolution by addition of concentrated HCl (37 %). To this solution was added $Na_2MoO_4{\cdot}2H_2O$ (0.050 g, 0.20 mmol) while maintaining the pH at 2.2 using 3 M HCl. Solid $Y(NO_3)_3{\cdot}6H_2O$ (0.0626 g, 0.163 mmol) was then added and the pH of the resulting solution was once again adjusted to 2.2. After allowing the reaction mixture to stand for one hour, *p*-MeBzNH$_2$ (50 µl, 0.39 mmol) was added and the reaction solution wrapped in foil and stored in the dark. Colorless tetrahedral-shaped crystals form overnight in 15 % yield (100 mg, 0.007 mmol) based on W. Structural analysis by X-ray crystallography affords the formula (*p*-MeBzNH$_3$)$_7$(L-Nle H)$_5$[As$_4$(Mo$^{VI}_3$)Mo$^{VI}_{2.5}$W$^{VI}_{41.5}$Y$_4$O$_{159}$(L-Nle)$_8$(H$_2$O)$_{11}$]·78H$_2$O (**3w**) for the wet crystals, which partially dehydrate upon drying. Anal. calcd (found) for air-dried **3**, $C_{134}H_{320}N_{20}As_4Mo_{5.5}W_{41.5}Y_4O_{216}$: C, 11.11 (11.3); H, 2.23 (2.3); N, 1.93 (2.0); As, 2.07 (2.0); Y, 2.46 (2.4); Mo 3.64 (3.3). Selected IR (KBr, cm^{-1}): 1731 (w), 1621 (s), 1500 (w), 1456 (w), 1432 (w), 1382 (w), 1339 (w), 955 (m), 859 (s), 805 (m), 720(m), 610 (s), 4821(w), 458 (w). ^{1}H NMR (400 MHz, D_2O): δ 0.92 (t, J = 8.0 Hz, 39H, CH_3), 1.39 (m, 52H, $(CH_2)_2$), 1.90 (m, 26H, CH_2), 2.38 (s, 21H, CH_3) 3.85 (t, J = 6.0 Hz, 13H, CH), 4.18 (s, 14H, CH_2), 7.33, 7.40 ppm (ABq, J = 8.0 Hz, 28H, ArH). ^{13}C{^{1}H} NMR (800 MHz, D_2O): δ 13.6 (CH_3),

21.0 (CH_3), 22.3 (CH_2), 27.0 (CH_2), 30.6 (CH2), 43.7 (CH_2), 55.0 (CH), 129.6, 130.3, 130.4, 140.3 (Ar), 174.9 ppm (COO).

(p-MeBzNH$_3$)$_7$(L-NleH)$_3$[As$_4$(Mo$^V_2$Mo^{VI}W^{VI})Mo$^{VI}_x$W$^{VI}_{44-x}$Y$_4$O$_{160}$(L-Nle)$_9$(H$_2$O)$_{11}$]·L-Nle·20H$_2$O (x = 1.5 (4a), 2 (4b), 2.5 (4c). Solid $K_{14}[As_2W_{19}O_{67}(H_2O)]$ (0.5263 g, 0.1000 mmol) was dissolved in 0.2 M norleucine (L-Nle, **4a-c**) solution (15 ml, 3.0 mmol) at pH 2.2, with this pH maintained during the dissolution by addition of concentrated HCl (37 %). To this solution was added $Na_2MoO_4{\cdot}2H_2O$ (0.040 g, 0.16 mmol) while maintaining the pH at 2.2 using 3 M HCl. Solid $Y(NO_3)_3{\cdot}6H_2O$ (0.0626 g, 0.163 mmol) was then added and the pH of the resulting solution was once again adjusted to 2.2. After allowing the reaction mixture to stand for one hour, hydrazinium sulfate solution (0.10 M; 200µl, 0.02 mmol, **4a**; 400µl, 0.04 mmol, **4b**; 800µl, 0.08 mmol, **4c**) was added and the solution left overnight. To the resulting dark blue solution was added p-$MeBzNH_2$ (50 µl, 0.39 mmol). Deep blue tetrahedral-shaped crystals form over the course of several days and one or two further crops can be collected after several weeks. Although spectroscopically identical, all of the physical studies reported herein were performed on the first crop.

(p-MeBzNH$_3$)$_7$(L-NleH)$_3$[As$_4$(Mo$^V_2$Mo^{VI}W^{VI})Mo$^{VI}_{1.5}$W$^{VI}_{42.5}$Y$_4$O$_{160}$(L-Nle)$_9$(H$_2$O)$_{11}$]·L-Nle·20H$_2$O (4a). Structural analysis by X-ray crystallography affords the formula (p-$MeBzNH_3$)$_7$(L-NleH)$_3$[As$_4$(Mo$^V_2$Mo^{VI}W^{VI})Mo$^{VI}_{1.5}$W$^{VI}_{42.5}$Y$_4$O$_{160}$(L-Nle)$_9$(H$_2$O)$_{11}$]·L-Nle·75H$_2$O (**4aw**) for the wet crystals, which partially dehydrate upon drying. Yield: 150 mg, 0.011 mmol (23 % based on W). Anal. calcd (found) for air-dried **4a**, $C_{134}H_{318}N_{20}As_4Mo_{4.5}W_{43.5}Y_4O_{217}$: C, 10.90 (11.4); H, 2.17 (2.2); N, 1.90 (1.9); As, 2.03 (1.98); Y, 2.41 (2.4); Mo 2.92 (2.6). Selected IR (KBr, cm^{-1}): 1731 (w), 1624 (s),1496 (m), 1460 (w), 1430 (w) , 1379 (w), 1344 (w), 955 (m), 861 (s), 808 (m), 765(m), 490 (w), 456 (w). ^{1}H NMR as per **4b**.

***(p*-MeBzNH$_3$)$_7$(L-NleH)$_3$[As$_4$(Mo$^V_2$Mo^{VI}W^{VI})Mo$^{VI}_2$W$^{VI}_{42}$Y$_4$O$_{160}$(L-Nle)$_9$(H$_2$O)$_{11}$]·L-Nle·20H$_2$O (4b).** Structural analysis by X-ray crystallography affords the formula (*p*-$MeBzNH_3$)$_7$(L-NleH)$_3$[As$_4$(Mo$^V_2$Mo^{VI}W^{VI})Mo$^{VI}_2$W$^{VI}_{42}$Y$_4$O$_{160}$(L-Nle)$_9$(H$_2$O)$_{11}$]·L-Nle·83H$_2$O (**4bw**) for the wet crystals, which partially dehydrate upon drying. Yield: 160 mg, 0.011 mmol (25 % based on W). Anal.

calcd (found) for air-dried **4b**, $C_{134}H_{318}N_{20}As_4Mo_5W_{43}Y_4O_{217}$: C, 10.93 (11.2); H, 2.18 (2.2); N, 1.90 (1.9); As, 2.04 (2.1); Y, 2.42 (2.4); Mo 3.26 (3.1). Selected IR (KBr, cm^{-1}): 1731 (w), 1617 (s), 1494 (w), 1456 (w), 1430 (w), 1382 (w), 1344 (w), 955 (m), 895 (s), 856 (s), 810 (m), 781(m), 737 (s), 765(m), 671 (s), 637(s), 490 (w), 456 (w). ^{1}H NMR (400 MHz, D_2O): δ 0.92 (m, 39H, CH_3), 1.38 (m, 52H, $(CH_2)_2$), 1.91 (m, 26H, CH_2), 2.38 (s, 21H, CH_3) 3.82 (t, *J* = 6.4 Hz, 13H, CH), 4.19 (s, 14H, CH_2), 7.33, 7.40 ppm (ABq, *J* = 8.4 Hz, 28H, ArH). ^{13}C{^{1}H} NMR (800 MHz, D_2O): δ δ 13.6 (CH_3), 20.9 (CH_3), 22.3 (CH_2), 27.0 (CH_2), 30.5 (CH2), 43.7 (CH_2), 54.9 (CH), 129.6, 130.3, 130.4, 140.3 (Ar), 174.8 ppm(COO).

(*p*-MeBzNH$_3$)$_7$(L-NleH)$_3$[As$_4$(Mo$^V_2$Mo^{VI}W^{VI})Mo$^{VI}_{2.5}$W$^{VI}_{41.5}$Y$_4$O$_{160}$(L-Nle)$_9$(H$_2$O)$_{11}$]·L-Nle·20H$_2$O (4c). Structural analysis by X-ray crystallography affords the formula (*p*-MeBzNH$_3$)$_7$(L-NleH)$_3$[As$_4$(Mo$^V_2$Mo^{VI}W^{VI})Mo$^{VI}_{2.5}$W$^{VI}_{41.5}$Y$_4$O$_{160}$(L-Nle)$_9$(H$_2$O)$_{11}$]·L-Nle·69H$_2$O (**4cw**) for the wet crystals, which partially dehydrate upon drying. Yield: 165 mg, 0.011 mmol (25 % based on W). Anal. calcd (found) for air-dried **4c**, $C_{134}H_{318}N_{20}As_4Mo_{5.5}W_{42.5}Y_4O_{217}$: C, 10.96 (11.3); H, 2.18 (2.3); N, 1.91 (2.0); As, 2.04 (2.1); Y, 2.42 (2.4); Mo 3.59 (3.2). Selected IR (KBr, cm^{-1}): 1731 (w), 1614 (s),1459 (w), 1440 (m), 1432 (w) , 1381 (w), 1344 (w), 952 (m), 893 (s), 856 (s), 813 (m), 760(s), 736 (s), 669(s), 640(s), 487 (w), 452 (w). ^{1}H NMR as per **4b**.

(*p*-MeBzNH$_3$)$_4$(DL-NleH)$_5${[As$_4$(Mo$^V_2$Mo^{VI}W^{VI})W$^{VI}_{44}$Y$_4$O$_{160}$(DL-Nle)$_8$(H$_2$O)$_{12}$]$_{0.5}$ [As$_4$(Mo$^{VI}_3$W^{VI})W$^{VI}_{44}$Y$_4$O$_{160}$(DL-Nle)$_8$(H$_2$O)$_{12}$]$_{0.5}$} DL-Nle 35H$_2$O (5). Synthesized as per **4b** using DL-Nle in place of L-Nle resulting in very thin square plate-like crystals overnight. Yield: 200 mg, 0.014 mmol (31 % based on W). Anal. calcd (found) for $C_{116}H_{329}N_{18}As_4Mo_3W_{45}Y_4O_{235}$: C, 9.32 (9.5); H, 2.22 (2.1); N, 1.69 (1.8); As, 2.00 (1.9); Y, 2.38 (2.9); Mo 1.92 (2.0). Selected IR (KBr, cm^{-1}): 1727 (w), 1619 (s), 1491 (w), 1456 (w), 1427 (w) , 1381 (w), 1341 (w), 957 (m), 859 (s), 816 (m), 730(s), 666(m), 621(s), 488 (w), 456 (w). ^{1}H NMR (400 MHz, D_2O): δ 0.92 (m, 42H, CH_3), 1.38 (m, 56H, $(CH_2)_2$), 1.92 (m, 28H, CH_2), 2.37 (s, 12H, CH_3) 3.90 (br, 14H, CH), 4.20 (s, 8H, CH_2), 7.33, 7.41 ppm (ABq, *J* = 8.0 Hz, 16H, ArH).

$(GlyH)_9K_3[As_4(Mo^{VI}_3)Mo^{VI}_{0.5}W^{VI}_{43.5}Y_4O_{159}(Gly)_8(H_2O)_{11}]\cdot(Gly)_6\cdot 15H_2O$ (6). Solid $K_{14}[As_2W_{19}O_{67}(H_2O)]$ (0.5263 g, 0.1000 mmol) was dissolved in 1 M glycine solution (20 ml, 20 mmol) at pH 2.2, with this pH maintained during the dissolution by addition of concentrated HCl (37 %). To this solution was added $Na_2MoO_4\cdot 2H_2O$ (0.040 g, 0.163 mmol) while maintaining the pH at 2.2 using 3 M HCl. Solid $Y(NO_3)_3\cdot 6H_2O$ (0.0626 g, 0.163 mmol) was then added and the pH of the resulting solution was once again adjusted to 2.2. The reaction flask was wrapped in foil and stored in the dark, affording colorless plate-like crystals overnight. These were recrystallized (in the dark) by dissolution in the minimum volume of water, followed by dilution with an equivalent volume of 1 M glycine (pH 2.2) to yield a mixture of square and rectangular plate-like crystals. Yield: 300 mg, 0.021 mmol (49 % based on W). Anal. calcd (found) for $C_{46}H_{176}N_{23}As_4Mo_{3.5}W_{43.5}Y_4O_{231}K_3$: C, 3.99 (4.2); H, 1.28 (1.4); N, 2.33 (2.4); As, 2.16 (2.2); Y, 2.57 (3.1); Mo 2.42 (2.1); K 0.85 (0.8). Selected IR (KBr, cm^{-1}): 1746(w), 1615 (s), 1481 (m), 1455 (m), 1410 (m), 1336 (w), 1310 (m), 1248(w), 1108(w), 951 (m), 862 (s), 800 (m), 717 (s), 616 (s), 489 (w), 460 (w). ^{1}H NMR (400 MHz, D_2O): δ 3.70 ppm (CH_2).

$(GlyH)_6K_{2.5}$ $\{[As_4(Mo^{V}_2Mo^{VI}W^{VI})Mo^{VI}W^{VI}_{43}Y_4O_{160}(Gly)_8(H_2O)_{12}]_{0.25}$ $[As_4(Mo^{VI}_3W^{VI})Mo^{VI}W^{VI}_{43}Y_4O_{160}(Gly)_8(H_2O)_{12}]_{0.75}\}$ $(Gly)_{14}\cdot 10H_2O$ (7a). Solid $K_{14}[As_2W_{19}O_{67}(H_2O)]$ (0.5263 g, 0.1000 mmol) was dissolved in 1 M glycine solution (20 ml, 20 mmol) at pH 2.2, with this pH maintained during the dissolution by addition of concentrated HCl (37 %). To this solution was added $Na_2MoO_4\cdot 2H_2O$ (0.040 g, 0.163 mmol) while maintaining the pH at 2.2 using 3 M HCl. Solid $Y(NO_3)_3\cdot 6H_2O$ (0.0626 g, 0.163 mmol) was then added and the pH of the resulting solution was again adjusted to 2.2 using 3 M HCl. After 10 minutes, hydrazinium sulfate solution (0.10 M, 400 µl, 0.163 mmol) was added, resulting in deep blue plate-like crystals overnight. These were recrystallized by dissolution in the minimum volume of water, followed by dilution with an equivalent volume of 1 M glycine (pH 2.2) to yield a mixture of square and rectangular plate-like crystals. Structural analysis of the rectangular plate-like crystals by X-ray crystallography affords the formula $(GlyH)_6K_{2.5}\{[As_4(Mo^{V}_2Mo^{VI}W^{VI})Mo^{VI}W^{VI}_{43}Y_4O_{160}(Gly)_8(H_2O)_{12}]_{0.25}$ $[As_4(Mo^{VI}_3W^{VI})Mo^{VI}W^{VI}_{43}Y_4O_{160}(Gly)_8(H_2O)_{12}]_{0.75}\}Gly)_{14}\cdot 49H_2O$ (**7aw**) for the wet crystals. The

sample partially dehydrates upon drying. Yield: 500 mg, 0.048 mmol (80 % based on W). Anal. calcd (found) for air-dried **7a**, $C_{56}H_{190}N_{28}As_4Mo_4W_{44}Y_4O_{238}K_{2.5}$: C, 4.71 (4.8); H, 1.34 (1.5); N, 2.74 (2.8); As, 2.10 (2.2); Y, 2.49 (2.8); Mo 2.69 (2.4); K 0.68 (0.8). Selected IR (KBr, cm^{-1}): 1735 (w), 1621 (s), 1492 (w), 1455 (w), 1429 (w), 1382 (w), 1322 (w), 955 (m), 890 (s), 856 (s), 810 (m), 780(m), 764(m), 738 (s), 671 (m), 664 (m), 639 (s), 487 (w), 455 (w), 433 (w). ^{1}H NMR (400 MHz, D_2O): δ 3.70 ppm (CH_2).

(p-MeBzNH$_3$)$_2$(GlyH)$_{7.5}${[As$_4$(Mo$^V_2$Mo^{VI}W^{VI})Mo$^{VI}_{1.5}$W$^{VI}_{42.5}$Y$_4$O$_{160}$(Gly)$_8$(H$_2$O)$_{12}$]$_{0.75}$ [As$_4$(Mo$^{VI}_3$W^{VI})Mo$^{VI}_{1.5}$W$^{VI}_{42.5}$Y$_4$O$_{160}$(Gly)$_8$(H$_2$O)$_{12}$]$_{0.25}$ }·(Gly)$_{12}$·30H$_2$O (7b). Dissolution of **4b** (67 mg, 0.0046 mmol) in the minimum volume of 1 M glycine (pH 2.2, *ca.* 1.5 ml) yields crystals of **7b** in 70% yield (47 mg, 0.0032 mmol) after 1 day. Structural analysis by X-ray crystallography affords the formula (p-MeBzNH$_3$)$_2$(GlyH)$_{7.5}${[As$_4$(Mo$^V_2$Mo^{VI}W^{VI})Mo$^{VI}_{1.5}$W$^{VI}_{42.5}$Y$_4$O$_{160}$(Gly)$_8$(H$_2$O)$_{12}$]$_{0.75}$ [As$_4$(Mo$^{VI}_3$W^{VI})Mo$^{VI}_{1.5}$W$^{VI}_{42.5}$Y$_4$O$_{160}$(Gly)$_8$(H$_2$O)$_{12}$]$_{0.25}$}·(Gly)$_{13}$·63H$_2$O (**7bw**), for the wet crystals, which partially dehydrate upon drying. Anal. calcd (found) for air-dried **7b**, $C_{71}H_{253}N_{29.5}As_4Mo_{4.5}W_{43.5}Y_4O_{257}$: C, 5.79 (6.3); H, 1.73 (1.7); 2.81 (2.5); As, 2.04 (1.9); Y, 2.42 (2.4); Mo 2.93 (2.5); K 0.00 (< 0.5). Selected IR (KBr, cm^{-1}): 1722 (w), 1632 (s), 1479 (w), 1412 (w), 1429 (w), 1384 (w), 1331 (w), 1253 (W), 1120 (W), 954 (m), 864 (s), 800 (m), 779(m), 760(m), 735 (s), 671 (m), 640 (s), 619 (m), 597(m), 513 (m), 490 (w), 455 (w). ^{1}H NMR (400 MHz, D_2O): δ 2.33 (s, 6H, CH_3), 3.70 ppm (s, 56H, CH_2), 4.15 (s, 4H, CH_2), 7.27, 7.36 ppm (ABq, J = 8.4 Hz, 8H, ArH).

X-ray Data Collection and Structure Solution. The crystallographic data (Table 1) for compounds **3w**, **4aw**, **4bw**, **4cw**, **7aw** and **7bw** (Figure S1) were collected on an Agilent Technologies SuperNova Dual Wavelength single crystal X-ray diffractometer using Cu-Kα radiation (λ = 1.5418 Å, mirror monochromated) at 130(2) K. The structures were solved by direct methods (SHELXT) and refined through full-matrix least-squares techniques on F^2 using SHELXL and OLEX2 crystallographic software packages.[61] [62] [63] All tungsten, molybdenum, yttrium and arsenic atoms were refined with anisotropic displacement parameters; all other atoms could only be refined isotopically. The

determination of the mixed metal composition of the polyanions (Figure S2) of **3w**, **4aw**, **4bw**, **4cw**, **7aw** and **7bw** is described in detail below.

3w: The $\{M_4\}$ "core" atom (Figure S2), assigned as Mo, showed anomalously high displacement parameters, suggesting partial occupancy. On refinement, the occupancy factor converged to 0.75, indicating that only 3 of the 4 core sites were occupied, the vacant site being equally distributed over 4 positions, due to the four-fold symmetry. The occupancy factor was fixed at 0.75 during the rest of the refinement. Some of the metal atoms associated with the $\{Y_4M_8L_8\}$ "ring" and the $\{AsM_9\}$ lacunary Keggin "triad" (Figure S2), originally assigned as W, also showed anomalously high displacement parameters, and partial occupancy on refinement. The chemical analysis indicated 5.5 Mo atoms for each POM, suggesting an excess of Mo (2.5 Mo atoms per POM) over that expected for just the "core" Mo atoms. Accordingly the metal atoms in the moiety associated with the $\{Y_4M_8L_8\}$ "ring" & those metal atoms in the $\{AsM_9\}$ lacunary Keggin "triad" were interpreted as being a mixture of W and Mo. None of the W atoms in the $\{AsM_9\}$ lacunary Keggin "belt" (Figure S2) showed significant deviation from full occupancy, and accordingly all were assigned as fully occupied W atoms during the rest of the refinement. The refinement converged with 5.9 Mo per POM (3 Mo in the core, and 2.9 distributed over the rest of the POM replacing W).

4aw: The "core" atom, originally assigned as Mo, showed anomalously small displacement parameters and, on refinement as Mo, the occupancy factor became greater than 1, suggesting that the site was a mixture of Mo and W (0.68 : 0.32 = 2.7 : 1.3). As the analysis showed 4.5 Mo per POM, the possibility that the core was composed of only partially occupied W atoms could be discounted as this would mean that all of the Mo would have to be distributed over the rest of the POM, rather than just 1.8 Mo per POM. As for **3w**, above, all metal atoms associated with the $\{Y_4M_8L_8\}$ "ring" and the $\{AsM_9\}$ lacunary Keggin "triad" showed partially occupancy, when refined as W, and accordingly refinement was continued with these sites being a mixture of W & Mo. Again, none of the W atoms in the $\{AsM_9\}$ lacunary Keggin "belt" showed significant partial occupancy and, accordingly, all were assigned full occupancy during the rest of the refinement.

4bw, **4cw**, **7aw** and **7bw**: The refinement of all four structures followed the same procedure for **4aw**, giving similar results, except that for **7aw** and **7bw** there seemed to be no significant substitution of Mo for W in the metal sites of the {AsM_9} lacunary Keggin "triad"; accordingly these metal atom sites were assigned to be fully occupied W. For **7aw**, the OLEX2 "Solvent Mask" procedure was used to remove the contributions of the disordered solvent.

For all six structures, the refinement was carried out with the atoms of the mixed Mo/W sites being constrained to the same position, with the same displacement parameters, and with the sum of the occupancy factors at each site being 1. The results from the structural analyses are consistent with the chemical analyses, given that there would be expected to be differences between the composition of a single crystal compared to the composition of a bulk sample. The positional disorder of the aliphatic chains of the Nle ligands in **3w**, **4aw**, **4bw** and **4cw** was modeled by restraining the components of the molecules to geometrical estimates. The composition of solvent voids was performed using the Platon software package,[64] on the basis of the chemical analyses of all compounds.

Table 1. Crystallographic Data for Compounds **3w**, **4aw**, **4bw**, **4cw**, **7aw** and **7bw**

	3w	**4aw**	**4bw**	**4cw**	**7aw**	**7bw**
Formula	$C_{134}H_{436}N_{20}As_4Mo_{5.5}W_{41.5}Y_4O_{274}$	$C_{134}H_{428}N_{20}As_4Mo_{4.5}W_{43.5}Y_4O_{272}$	$C_{134}H_{444}N_{20}As_4Mo_5W_{43}Y_4O_{280}$	$C_{134}H_{416}N_{20}As_4Mo_{5.5}W_{42.5}Y_4O_{266}$	$C_{56}H_{308}N_{28}As_4Mo_4W_{44}Y_4O_{297}K_{2.5}$	$C_{71}H_{319}N_{29.5}As_4Mo_{4.5}W_{43.5}Y_4O_{290}$
Formula weight / g mol^{-1}	15526	15757	15858	15561	15354	15312
Crystal system	cubic	cubic	cubic	cubic	monoclinic	monoclinic
Space group	*F*432	*F*432	*F*432	*F*432	$P2_1/n$	$P2_1/n$
a / Å	59.6589(7)	60.0131(9)	59.000(3)	59.9036(5)	29.9904(3)	29.9530(3)
b / Å	-	-	-	-	30.7970(5)	30.8650(4)
c / Å	-	-	-	-	30.0257(3)	30.2803(3)
α	-	-	-	-	-	-
β	-	-	-	-	90.2392(10)	90.1117(8)
γ	-	-	-	-	-	-
V / Å^3	212337(4)	216142(6)	211313(4)	214961(3)	27731.8(6)	27994.1(5)
Z	24	24	24	24	4	4
T / K	130	130	130	130	130	130
ρ_{calc} / g cm^{-3}	2.914	2.905	2.985	2.893	3.677	3.633
μ / mm^{-1}	27.960	28.327	28.796	28.244	37.355	36.471
reflns measd	49103	22220	43885	41467	200569	197531
unique reflns	18268	5208	16529	16389	55545	56966
Data/ restraints/ parameters	18268/15/383	5208/10/391	16529/5/386	16389/4/404	55545/2/1356	56966/2/1363
R_{int}	0.0428	0.0772	0.0468	0.0547	0.098	0.0714
R_1 [$I > 2\sigma(I)$]	0.0905	0.0657	0.0585	0.0655	0.0997	0.0721

wR_2 (all data)	0.3431	0.1806	0.1733	0.1915	0.2968	0.2174
Goodness-of-fit on F^2	1.040	1.093	1.069	1.030	1.022	1.020
$\Delta\rho_{max,min}$ / e Å^{-3}	1.18/-1.09	1.29/-1.27	1.45/-1.72	1.73/-2.37	9.59/ -2.72	4.78/-3.11

Electrochemistry. Cyclic and steady state rotating disk electrode (RDE) voltammetric experiments were carried out in DMSO with Bu_4NPF_6 (0.05 M) as the supporting electrolyte or in aqueous 0.2 M Gly buffer at pH 2.2. A standard three-electrode cell configuration was employed using 3 mm diameter glassy carbon (or glassy carbon RDE) working electrode and a Pt wire auxiliary electrode. A Ag/AgCl (3 M NaCl) reference electrode was used in aqueous solutions, while an Ag wire quasi-reference electrode separated from the analyte solution by a sintered glass frit filled with the electrolyte solution was used in DMSO solution. The potential of the Ag quasi-reference electrode was calibrated against the ferrocene/ferricenium ($Fc^{0/+}$) couple and all potentials are reported with respect to this reference scale. Controlled potential electrolysis was performed in a two-compartment cell equipped with a large area glassy carbon plate as the working electrode, a platinum mesh as counter electrode and the same reference electrode as used in voltammetric experiments. Freshly prepared solutions were used for all electrochemical measurements.

Small Angle X-ray Scattering (SAXS). Data were collected on a Bruker MicroCalix instrument, using Cu-Kα radiation at a wavelength of 1.54 Å. The instrument was run in high flux mode, with the X-ray microsource running at 50 W. Scattered X-rays were detected using a Pilatus 100k detector. Solutions of known concentration were measured in 0.5 or 1.5 mm diameter quartz X-ray capillaries with 10 μm wall thickness (Hilgenberg, Germany). Scattering and transmission measurements were made for each of the samples, as well as for a sample containing only the blank solution. Scattering patterns were collected for 180 minutes, and transmission measurements for 5 s. Initial data processing (normalization, primary beam masking, and background subtraction) was carried out in fit-2D. No smoothing was used, and the data quality was not significantly affected by normalization. Scattering curves were recorded in

the range (0.06-0.6 $Å^{-1}$). A low q (0.06-0.17 $Å^{-1}$) Guinier analysis was carried out using ATSAS 2.7.0, yielding an independent measure of the radius of gyration (R_g) and forward scattering (I_0). For comparison to the solution experimental data, the SolX computer program was used to calculate theoretical scattering patterns and R_g values using single crystal X-ray diffraction data as input.[65,66] Pair distance distribution functions (PDDFs) were obtained from fits to the $I(q)$ data using the inverse Fourier transform (FT) method of Moore[67] as implemented in the Irena software package for Igor Pro.

Other Measurements. Infrared spectra (KBr disk) were recorded on a Bruker Tensor 27 FTIR spectrometer. X-ray photoelectron (XPS) spectra were recorded on a Thermo Scientific K-Alpha Photoelectron Spectrometer system with a monochromated, micro-focused Al K-α X-ray source. Calibration of all spectra was attained by reference to the carbon 1s signal with a binding energy of 285.0 eV. A small degree of X-ray induced photoreduction was observed during data acquisition, with the Mo^{V}/Mo^{VI} ratio gradually increasing over many scans for all compounds, especially the oxidized species **3** and **6**. All elemental analyses were performed at the Campbell Microanalytical Laboratory, University of Otago; the CHN analyses employed a Carlo Erba Elemental Analyser EA 1108, while ICP-MS analyses for As, K, Mo and Y employed an Agilent Technologies 7500ce quadrupole ICP-MS. Electronic absorption was measured on an Agilent Technology Cary60 UV-Visible spectrometer and reflectance spectra were measured on a Thermo Scientific-Evolution 220 UV-Visible spectrometer. Circular dichroism (CD) spectra were measured on an Aviv Model 410SF spectrometer and spectra were obtained by averaging 8 spectra with a scanning speed of 30 nm min^{-1}. ^{1}H NMR spectra were acquired on a Varian MR400 400 MHz spectrometer and referenced to residual HDO. $^{13}C\{^{1}H\}$ and ^{1}H-^{13}C NMR spectra were acquired on a Bruker Avance-II-800MHz spectrometer and referenced to MeOH.[68]

Computational details. Density functional theory (DFT) calculations were carried out on structures based on the title compounds. The computed structures include the full inorganic part of the polyanions, whereas the amino acid ligands are replaced by formate groups. This simplification considerably reduces the computational time without affecting the quality of the results of interest nor the conclusions provided by the quantum chemical analysis. We used the ADF2013.01 suite of programs[69] to get optimized geometries and molecular energies applying the BP86 functional, and to draw 3D representations of the molecular orbitals.[70] The valence electrons of all atoms were described by triple- ζ + polarization (TZP) Slater-type basis sets, with a total of ~7000 Cartesian basis functions per molecule. Internal or *core* electrons (C, O: 1s; As: 1s-3d; Mo: 1s-4p; W: 1s-4f; Y: 1s-4p) were kept frozen, each described by a single Slater function (1870 in total) with core potentials generated using the DIRAC program.[64a] Scalar relativistic corrections were included by means of the zeroth-order regular approximation (ZORA) and solvent effects of water (characterized by the dielectric constant ε = 78.4) with the *conductor-like screening model* (COSMO[71]) at every SCF cycle of the computation.

Results and Discussion

Syntheses. The general procedure for the synthesis of the $[As_4(M_4)Mo^{VI}_xW^{VI}_{44-x}Y_4O_{160}(AA)_y(H_2O)_z]^{n-}$ family involves dissolution of $K_{14}[As_2W_{19}O_{67}(H_2O)]$ in a solution of the appropriate amino acid with maintenence of the pH at 2.2. Sodium molybdate is added for the Mo-containing analogs, followed by yttrium nitrate, affording a clear solution. In the presence of Mo, the solution immediately begins to turn blue due to photoreduction by ambient light. The previously reported synthesis of norleucine compound **2** involves exposure to a UV lamp overnight to generate a photoreduced solution, with norleucine the likely electron donor.

Addition of *p*-$MeBzNH_3^+$ cations to the blue solution yields **2** as a crystalline product. We have subsequently rationalized that the nature of compound **2** as a mixture of POMs in two redox states, the fully oxidized homovalent M^{VI} (M = Mo and W) species and the 2e-reduced $\{Mo^V_2\}$-containing analog, probably results from the fact that the compound begins to crystallize from solution before all polyanions are reduced. In an effort to overcome this and access our initial target of a fully 2e-reduced $\{Mo^V_2\}$-containing POM, we turned to chemical rather than photoreduction, selecting hydrazinium sulfate as a convenient reductant because of its reasonable stability and successful employment in the synthesis of other reduced POMs.[21] As well as varying the amount of hydrazinium, we also varied the amount of added molybdate in a targeted effort to obtain the tetra-substituted 2e-reduced $[As_4(Mo^V_2Mo^{VI}_2)W_{44}Y_4O_{160}(AA)_x(H_2O)_y]^{n-}$ analog, rather than species with mixed metals in the central tetranuclear core. This target theoretically requires 1.74 mole equivalents of molybdate and 0.22 mole equivalents of hydrazinium per $[As_2W_{19}O_{67}(H_2O)]^{14-}$, given that hydrazinium is formally a 4e-reductant and assuming complete conversion of the POM precursor to the hybrid POM product. However, multiple equilibria appear to be involved in the formation of the hybrid POM in solution and we found that the use of stoichiometric molybdate in fact affords products with more than four Mo centers per POM (see later) and that for a given amount of molybdate, variation of the amount of hydrazinium controls the extent of incorporation of Mo. Ultimately we settled on 1.6 mol equivalents of Mo and 0.22, 0.44 and 0.87 mol equivalents of hydrazinium to explore norleucine analogs with 4.5 (**4a**), 5 (**4b**) and 5.5 (**4c**) Mo atoms per hybrid POM, respectively. These compounds are obtained in moderate yields as homogeneous crystalline samples of tetrahedral-shaped crystals (Figure S1). Redissolution and ^1H NMR spectroscopy indicate that all samples are diamagnetic. Although a considerable excess of hydrazinium is used, coulometry suggests

that the products are 1.8(2) electron reduced (see later), apparently always a little short of the target 2e-reduced, although for simplicity, these **4a**, **4b** and **4c** are formulated herein as comprised of only the 2e-reduced $\{Mo^{V}_{2}\}$-containing analog. The use of more hydrazinium in attempts to access a further reduced species affords a green-blue solution from which crystals could not be obtained. Synthesis of the racemic DL-norleucine-containing analog **5** was performed using the same amounts of molybdate and hydrazinium as **4b**, affording crystals of a different morphology to **4b**, which were unsuitable for single crystal X-ray diffraction. The infrared and electronic absorption spectra of **5** (see later) suggest that it is overall less reduced than **4b**, coulometric oxidation (see later) gives a valaue of approximately 1.3(2) electrons per POM and ^{1}H NMR indicates that the sample is diamagnetic. These data are interpreted as a sample comprised of a mixture of two hybrid polyanions with different redox states: the fully oxidized homovalent M^{VI} (M = Mo and W) species and the 2e-reduced $\{Mo^{V}_{2}\}$-containing analog. For simplicity, **5** is formulated as comprised of an equal mixture of oxidized and 2e-reduced hybrid POMs.

The synthesis of the reduced glycine-containing analog (**7a**) essentially parallels that of the norleucine-containing analogs, although a higher concentration of glycine is required, as the use of a lower concentration of glycine instead gives rise to an analog of a previously reported different compound.[59] The amount of hydrazinium again affects the extent of Mo substitution, with **7a** obtained following the use of the same ratio of molybdate : hydrazinium: $K_{14}[As_2W_{19}O_{67}(H_2O)]$ as employed for **4b**. In the case of **7a**, recrystallization of the crude product is required to generate crystals suitable for single crystal X-ray diffraction, affording a mixture of rectangular and square plate-like crystals. Samples of **7a** for all studies reported herein were similarly recrystallized. The degree of reduction of **7a** was determined by

coulometry as approximately 0.7(2) electrons per POM, and is consistent with the extinction coefficients determined from electronic absorption spectroscopy (see later). Compound **7a** is also diamagnetic and is thus formulated as a 3:1 mixture of oxidized and 2e-reduced hybrid POMs.

Circular dichrosim experiments (see later) suggested the possibility of exchanging glycine and norleucine ligands and subsequently Gly-containing **7b** was obtained in good yield by recrystallizing Nle-containing **4b** from 1 M glycine. Compound **7b** is significantly darker in color than **7a**, indicating that it has a higher proportion of the 2e-reduced POM. The degree of reduction of **7b** was determined by coulometry as approximately 1.5(2) electrons per POM, and is consistent with the extinction coefficients determined from electronic absorption spectroscopy (see later). The lesser degree of reduction found for **7b** than the parent **4b** suggests that partial oxidation has accompanied the recrystallization step. ^{1}H NMR spectroscopy of **7b** confirms complete exchange of the norleucine ligands for glycine. Compound **7b** is thus formulated as a 1:3 mixture of oxidized and 2e-reduced hybrid POMs.

The possibility of isolating samples comprised of only the oxidized Mo^{VI}-containing hybrid POM became apparent during the synthetic explorations of the reduced analogs described above. Both Nle-containing oxidized analog **3** and Gly-containing analog **6** are synthesized without addition of a reductant, with the early addition of *p*-$MeBzNH_3^+$ cations key in the case of **3**. In both cases, the reaction, and in the case of **6**, recrystallization solutions, are covered by aluminum foil and kept in the dark to avoid photoreduction, although the top of the flask is not sealed to allow a certain degree of evaporation. Solutions of both **3** and **6** are susceptible to photoreduction by ambient light, although **6** photoreduces significantly more rapidly than **3**. The crystals (Figure S1) of **2**, **3**, **4a**, **4b** and **4c** all exhibit a tetrahedral morphology, while **6**, **7a** and

7b are comprised of a mixture of square and rectangular plate-like crystals. However while the reduced species **2**, **4**, **5** and **7b** are deep blue in color and **7a** is medium blue, the crystals of oxidized **3** and **6** exhibit a very faint blue tint, which is likely due to a small degree of photoreduction on the crystal surface.

Solid State Studies: Composition Determination and General Comments. Bulk samples of the compounds are crystalline and homogeneous to the eye and all were characterized by elemental analysis, IR and XPS spectroscopy. A single crystal type was evident in all of the Nle-containing compunds, while two crystal types where present in the Gly-containing compounds **6** and **7a**, only one of which was amenable to characterization by single crystal X-ray diffraction. Wherever possible, single crystal diffraction data were collected for multiple crystals from different batches to test reproducibility from batch to batch and also homogeneity within a batch. The single crystal data were generally in agreement with the bulk analytical data, with crystal to crystal variations of less than 10 % in the site-specific Mo/W occupancy values (see later). Metal analyses indicated 5.5, 4.5, 5, 5.5 and 3 Mo centers per hybrid POM for norleucine-containing **3**, **4a**, **4b**, **4c** and **5**, respectively (Table 2). Glycine-containing **6**, **7a** and **7b** analyzed for 3.5, 4 and 4.5 Mo centers per molecule. The single crystal data reported herein are for individual crystals of **3w**, **4aw**, **4bw**, **4cw**, **7aw** and **7bw** with respectively, 5.9, 4.6, 5, 5.5, 4.6 and 4.8 Mo atoms per hybrid POM (Table 2). The formulations given for all compounds reflect the average composition of the bulk samples based on the elemental analysis and ^{1}H NMR spectra, combined with the degree of reduction determined from electrochemical and spectroscopic data (see later). As reported previously, magnetic susceptibility and EPR measurements performed on solid samples of the reduced compounds indicate that they are diamagnetic, consistent with the solution ^{1}H NMR spectroscopy.

Table 2. Selected interatomic distances (Å) and angles (˚) associated with $\{M_3\}$ or $\{M_4\}$ core, Mo site occupancies (%) for disordered Mo/vacancy and Mo/W sites and number of Mo per POM from crystallography and elemental analysis for **3w**, **4aw**, **4bw**, **4cw** and **7aw**.

	3w	**4aw**	**4bw**	**4cw**	**7aw**	**7bw**
Interatomic parameters						
M=O	1.75(6)	1.74(5)	1.70(2)	1.73(4)	1.68(2)-1.71(2)	1.68(1)-1.73(1)
M-O_{aqua}	2.31(5)	2.19(5)	2.17(2)	2.27(4)	1.98(3)-2.21(2)	2.15(2)-2.18(2)
M-O(-M)	1.92(4)-1.96(4)	1.86(4)-1.94(4)	1.88(2), 1.89(2)	1.90(4)-1.92(4)	1.88(2)-1.97(2)	1.89(1)-1.93(1)
O-M-O (O=M-OH_2)	175(2)	178(2)	174(1)	176(2)	171(1)-176(1)	174.1(6)-175.8(6)
O-M-O	93(3)	94(2)	94(1)	93(2)	92(1)-96(1)	92.9(5)-93.6(5)
M-O-M	125(2)	141(2)	143(1)	141(2)	134(1)-137(1)	138.2(7)-139.0(7)
M···M (M-O-M)	3.448(8)	3.583(8)	3.567(3)	3.594(7)	3.545(2)-3.550(2)	3.563(1)-3.576(2)
M···M (diagonal)	4.875(8)	5.067(8)	5.045(2)	5.083(7)	4.978(2)-5.054(2)	5.040(2)-5.053(2)
Mo occupancies (%)						
$\{M_3\}$ or $\{M_4\}$ core	75(0) [a]	68(3)	81(2)	80(3)	88(1)	86(1)
$\{Y_4M_8L_8\}$ "ring" [b]	25(1)	16(2)	17(1)	23(2)	14(1)	17(0)
$\{AsM_9\}$ "triad" [b]	7(2)	5(2)	3(1)	4(2)	0	0
$\{AsM_9\}$ "belt" [b]	0	0	0	0	0	0
W occupancies (%)						
$\{M_3\}$ or $\{M_4\}$ core	0[1]	32(3)	19(2)	20(3)	12(1)	14(1)
$\{Y_4M_8L_8\}$ "ring" [b]	75(1)	84(2)	83(1)	77(2)	86(1)	83(0)
$\{AsM_9\}$ "triad" [b]	93(2)	95(2)	97(1)	96(2)	100	100
$\{AsM_9\}$ "belt" [b]	100	100	100	100	100	100
Total core occupancy	3	4	4	4	4	4
Total Mo per POM						
crystallography (sum of Mo occupancies)	5.9	4.6	5	5.5	4.6	4.8
elemental analysis (bulk)	5.5	4.5	5	5.5	4	4.5

[a] Mo/vacancy disorder, all other values are for Mo/W disorder. [b] see Figure S2

Structural Analysis. Single crystal X-ray diffraction data (Table 1) indicate that Nle-containing compounds **3w**, **4aw**, **4bw** and **4cw** are isomorphous with previously reported compound **2**, crystallizing in the enantiomorphic cubic space group F432. The rectangular plate-like crystals of the Gly-containing compounds **6**, **7aw** and **7bw** are isomorphous and crystallize in the monoclinic space group $P2_1/n$; although a high quality data set could be obtained for these crystals of **7**, it was not possible for **6**. The square plate-like crystals of **6**, **7aw** and **7bw** were very poorly diffracting, although in all three cases they appear to be isomorphous and belong to the triclinic space group P-1 with similar unit cells (a = 16.800(3), b = 28.740(6), c = 30.070(3) Å; α = 83.00(3), β = 77.54(3) γ = 77.90(3) °). The structure of the hybrid POMs in each compound are based on the $[As_4(M_4)Mo^{VI}_xW^{VI}_{44-x}Y_4O_{160}(AA)_y(H_2O)_z]^{n-}$ (M = Mo/W) generic unit, with four tri-lacunary α-Keggin $\{AsM_9\}$ moieties linked by a $\{Y_4M_8L_8\}$ "ring" fragment (L = zwitterionic Gly, **6,** and **7**; L-Nle , **3** and **4**) with an inner oxo-bridged "core" (Figures 2 and S2). Two types of zwitterionic amino acid ligands bridge pairs of W centers or pairs of Y centers via carboxylate groups (Figure S3), with the protonated amine groups involved in intramolecular hydrogen bonding to the $\{AsM_9\}$ fragments with N(-H)···O distances of 2.8-3.0 Å. The $\{M_4\}$ core metal centers have trans oxo-aqua terminal ligands, with a ninth monodentate norleucine ligand disordered with these aqua ligands in the Nle-containing reduced compounds **4aw**, **4bw** and **4cw** (Figure S3).

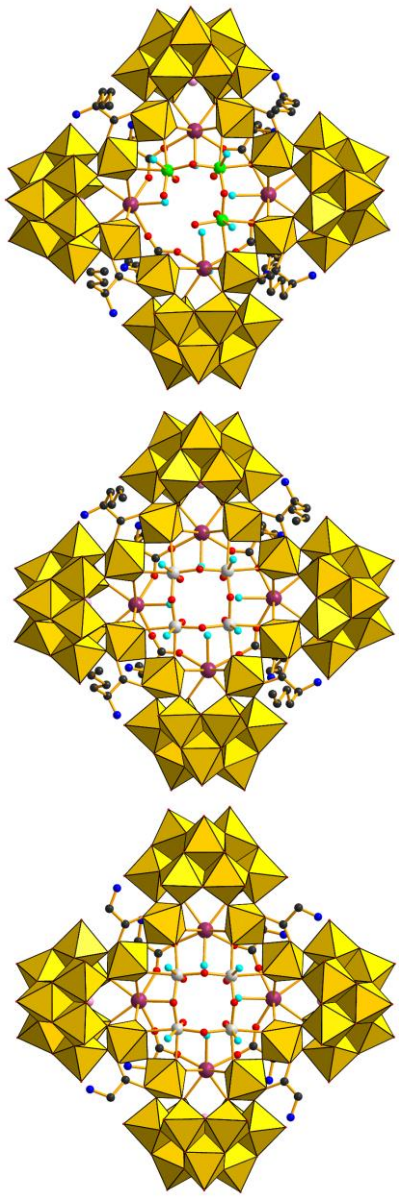

Figure 2. Structural representations of the molecular structure of: (top) **3**, (middle) **4b** and (bottom) **7b**. Color code as per Figure 1 and Mo, green.

An intriguing difference is that while compounds **2**, **4aw**, **4bw**, **4cw, 7aw** and **7bw** exhibit the expected $\{M_4\}$ core (M = disordered Mo and W), the oxidized homovalent M^{VI} (M = Mo, W) analog **3w**, which is isomorphous to **2**, **4aw**, **4bw** and **4cw**, possesses a monovacant

{Mo_3} core (Figure 2), with 75 % Mo occupancy for each of the four sites and no tungsten. Although a high quality X-ray data set could not be obtained for **6**, it is formulated herein with a trimetallic core by analogy with the other fully oxidized species, **3w**, and this formulation is supported by the similarity of the IR spectra of the two compounds (see later) in comparison to the spectra of the reduced analogs, as well as DFT calculations (see later). However, this formulation requires better crystallographic data to be definitive.

Close inspection of the single crystal X-ray diffraction data of all analogs reveals disorder of Mo/W in many of the metal positions, with the site occupancies summarized in Table 2. Incorporation of Mo into the metal positions shows considerable selectivity, with the Mo site occupancy decreasing in the same order for all analogs: {M_4} or {M_3} core > {$Y_4M_8L_8$} "ring" > {AsM_9} "triad" > {AsM_9} "belt" (Figure S2). A significant preference for the inner {M_4} or {M_3} core is evident with between 68 and 88 % Mo occupancy. In no case is any Mo evident in the "belt" positions of the {AsM_9} units. These occupancies can be interpreted in terms of the likely disassembly/reassembly from the $[As_2W_{19}O_{67}(H_2O)]^{14-}$ precursor, with the smallest extent of Mo for W exchange during complex formation occurring in the tri-lacunary α-Keggin {AsW_9} fragments that are present in the POM precursor.

Bond valence sum (BVS) calculations are challenging for species with mixed-metal site occupancies,[72] especially for those that are also mixed-valence, with this caveat in mind the BVS values for the cores of compounds **4aw**, **4bw**, **4cw**, **7aw** and **7bw** are consistent with oxidation states between penta- and hexavalent, while the other W/Mo positions are hexavalent for all compounds. Bond valence sum calculations on all bridging oxo ligands for all compounds give values in the range 1.7-2.2, consistent with an absence of localized protonation to hydroxo ligands.[73] It must be noted that while reduced compounds **4a**, **4b** and **4c** are formulated with 2e-

reduced $\{Mo^{V}_{2}Mo^{VI}W^{VI}\}$ cores, it is impossible to experimentally distinguish between this situation and same equal mix of compounds with 2e-reduced $\{Mo^{V}_{2}Mo^{VI}_{2}\}$ and $\{Mo^{V}_{2}W^{VI}_{2}\}$ cores. Spectroscopic and electrochemical data (see later) indicate that compounds **5**, **7a** and **7b** are mixtures of different proportions of fully oxidized homovalent M^{VI} (M = Mo, W) and 2e-reduced $\{Mo^{V}_{2}\}$-containing complexes; all compounds are diamagnetic. It is notable that single crystal X-ray diffraction data for all photo- and/or chemically reduced mixed Mo/W analogs of this family of compounds exhibit full occupancy of the tetranuclear core, indicating there is no component with a trinuclear core as is observed for oxidized species **3**.[55,74] Given no evidence for a component with a trinuclear core and core Mo occupancies in the range 68-88 %, "partially-reduced" compounds **5**, **7a** and **7b** are formulated as mixtures of complexes with hexavalent $\{Mo^{VI}_{3}W^{VI}\}$ and 2e-reduced mixed-valent $\{Mo^{V}_{2}Mo^{VI}W^{VI}\}$ tetrametallic cores.

Comparison of the diffraction data for compounds **3w**, **4aw**, **4bw**, **4cw**, **7aw** and **7bw** provides insight into the effects on the POM molecular structure of (i) different degrees of reduction, (ii) tri- versus tetrametallic core and (iii) norleucine versus glycine ligands. In all compounds the outer framework comprised of four tri-lacunary α-Keggin $\{AsM_9\}$ moieties linked by the cyclic $\{Y_4M_8L_8\}$ fragment is conserved, with little structural variation and essentially no dependence on the nature of the amino acid ligand, the nuclearity of the inner core or the variation in Mo/W occupancies. The more flexible part of the structure is the central core and it is intriguing that while a tetrametallic core is obtained for all reduced species, in the absence of reduction a trimetallic $\{Mo_3\}$ core is obtained in the case of Nle-containing **3w** or a highly distorted $\{W_3Y\}$ core in the case of previously reported fully oxidized Gly-containing **1**. It is curious that a homo-tetrametallic $\{Mo_4\}$ or $\{W_4\}$ compound is yet to be definitively characterized for any analog of this structural family. This may reflect the specific size and

binding characteristics of this structural pocket and subtle differences in ionic radii between M^{VI} and M^{V} (M = Mo, W). The most notable structural differences between the trimetallic fully oxidized core of **3w** and the tetrametallic reduced cores of **4aw**, **4bw**, **4cw** are the shorter M···M separations and more acute M-O-M angles for **3w** (Table 2), reflecting an overall smaller central core in this compound.

As was observed previously for **1** and **2**, the Nle- and Gle-containing analogs differ in the arrangement of the amino acid ligands (Figure S4). For isomorphs **2**, **3w**, **4aw**, **4bw** and **4cw** the four Nle ligands that bridge W centers rotate in the opposite sense to the four that bridge Y centers. In contrast, for Gly-containing compounds **1**, **7aw** and **7bw** all eight Gly ligands are oriented in the same direction. This is despite the fact that compounds **1** and **7aw** /**7bw** exhibit different crystal packing, with **1** incorporating *p*-$MeBzNH_3^+$ ligands that are absent in **7aw**/**7bw**. The arrangement of the Nle ligands in the Nle-containing compounds likely reflects both the necessity of accommodating relatively hydrophobic *n*-butyl chains and the different crystal packing.

The isomorphous Nle-containing compounds **2**, **3w**, **4aw**, **4bw** and **4cw** crystallize in the chiral space group *F*432, with each crystal comprised of one enantiomeric form of the polyanion. The polyanions pack such that they occupy the six faces of approximately cubic-shaped cavities, which are lined by the *n*-butyl chains of Nle ligands (Figure S5). The differing "top" and "bottom" faces of the disk-like polyanions give rise to two types of these cavities. The contents of both of these cavities, as well as the channels of that run in all three directions, are crystallographically disordered. Approximate void calculations using the Platon software package[64] results in total void volumes consistent with the accommodation of the cations, free amino acid and water molecules of hydration given in the formulations of **3w**, **4aw**, **4bw** and

4cw. The closest intermolecular W···W separation in Nle containing compounds is 6.1 Å. In contrast to the Nle-based analogs, the polyanions in the Gly-containing compound **7** pack in offset alternating double layers (Figure S6). The closest intermolecular W···W separation is 5.9 Å and there are no intermolecular hydrogen bonding interactions between polyanions. Again the cations, free glycine and hydrate molecules are disordered and the calculated total void volume is consistent with the formulation of **7aw** and **7bw**.

Infrared Spectroscopy. Infrared spectra were acquired for compounds **3**, **4a**, **4b**, **4c**, **5**, **6, 7a** and **7b** as pressed KBr disks. The spectra for all compounds exhibit bands consistent with the presence of the amino acid ligands and organic cations (Figure S7). Comparison of the fingerprint region below 1100 cm^{-1} is informative (Figure S8), as this region is dominated by the intense absorption bands of the inorganic POM backbone. The spectra for oxidized compounds **3** and **6** are very similar, with five broad bands in the region 550-1000 cm^{-1}. Four of these bands between 650 and 1000 cm^{-1} strongly resemble the spectrum of the $K_{14}[As_2W_{19}O_{67}(H_2O)]$ precursor and are assigned as follows: the band at ~ 950 cm^{-1} is attributed to the terminal M=O (M = Mo, W) stretch, the broad band at 860 cm^{-1} with a shoulder at 900 cm^{-1} is due to the corner-sharing M-O-M stretches and the two bands at 720 and 800 cm^{-1} are due to edge-sharing M-O-M stretches, possibly overlapping with the As-O-M stretches.[75] The strong similarity between the spectra of the two oxidized compounds **3** and **6** supports the proposition that the trimetallic core that is crystallographically observed for **3** is likely also be present in the non-crystallographically characterized **6**. Upon reduction, spectral changes are evident for both Nle- and Gly-containing analogs **4**, **5** and **7** with the tetrametallic core. Between 820 and 1000 cm^{-1} the spectra resemble those of the oxidized species, with the addition of a shoulder at around 970 cm^{-1}. Below 820 cm^{-1}, the three bands evident for **3** and **6** appear to be split, broadened and shifted for the reduced

analogs **4**, **5** and **7**. Shifting of M-O-M stretching bands and spectral broadening upon reduction has been observed previously for several POMs, with the extent of broadening dependent on the degree and site of localization/delocalization of the reducing electrons. [76-80] The subtle difference between the spectra for **4a**, **4b** and **4c** presumably arise from the small differences in Mo content. It is notable that the spectrum of **5** appears intermediate between those of oxidized **3** and 2e-reduced **4**, consistent with a mixture of the two oxidation states. The spectra of both **7a** and **7b** appear to combine some of the features of **3** and **6** with the increased spectral complexity in the 550 to 700 cm^{-1} range that is evident for **4** and **5**. The spectra are qualitatively consistent with **7a** and **7b** both being comprised of a mixture of oxidized and 2e-reduced hybrid POMs, with a higher proportion of oxidized POM in **7a** than **7b**.

X-ray Photoelectron Spectroscopy (XPS). X-ray photoelectron spectra were measured for representative oxidized compounds **3** and **6** and reduced compounds **4b** and **7a**. The W 4f and Mo 3d spectra are available in Figure S9 and the binding energies from spectral deconvolution are tabulated in Table S1. Literature binding energies for the W $4f_{7/2}$ and $4f_{5/2}$ peaks average around 35.5 and 37.9 eV for W^{VI} and 34.1 and 36.7 eV for W^{V}.[81,82] The W 4f spectra for **3**, **6**, **4b** and **7a** all exhibit only the doublet associated with W^{VI} at binding energies of 35.8-36.6 and 37.9-38.7 eV, with no indication of any W^{V} or W^{IV} in any of the compounds. The signal to noise is much poorer for the molybdenum spectra, due to the relatively small amounts of Mo in each of the compounds. Literature binding energies for the Mo $3d_{5/2}$ and $3d_{3/2}$ peaks average around 232.7 and 235.9 eV for Mo^{VI}; 231.5 and 234.2 eV for Mo^{V} and 229.5 and 233.0 eV for Mo^{IV}. [50,81,83,84] We have previously found that the Mo-containing analog **2** was photoreduced during XPS measurements, with the reduction taking place at the Mo sites and apparent in the Mo spectra. Similar photoreduction was observed for the present compounds,

with all compounds exhibiting spectra that can be deconvoluted to give components characteristic of Mo^{VI} and Mo^{V}, with Mo^{VI} doublets in the ranges 232.4-233.3 and 236.0-236.5 eV and Mo^{V} doublets in the range 231.2-233.1 and 234.1-235.6 eV. The amount of Mo^{V} increases at the expense of Mo^{VI} as the number of scans increases. Confining our analysis to the minimum number of scans required for reasonable signal to noise, we can semi-quantitatively confirm that reduced compounds **4b** and **7a** have more Mo^{V} than do oxidized compounds **3** and **6**. The tungsten and molybdenum XPS spectra definitively confirm that reduction takes place site selectively at molybdenum rather than tungsten centers.

Solution Studies: Determination of Solution Structure and Stability. Determination of the degree (and site) of reduction of the reduced hybrid POMs in this study is essential to establish their chemical formulas. Measuring the degree of reduction is best achieved by coulometry, however, for the results of electrochemical studies to be meaningful, it is first necessary to establish the stability of the hybrid POM in solution. In the present study, multiple physical techniques were employed for this purpose. In the first instance, electronic absorption spectroscopy of the reduced compounds provides a simple probe for monitoring changes in the degree of reduction over time. Small angle X-ray scattering allows establishment of the size and shape of the metal-oxo POM framework. Circular dichroism and ^{1}H NMR spectroscopy provide information on the amino acid ligands of the hybrid POMs.

The solubility properties of the different analogs depend on the amino acid, degree of reduction and overall charge. In our initial explorations of solution properties we opted to redissolve the compounds in aqueous solution at pH 2.2-2.4, which is the pH at which the compounds crystallize. In all cases, dissolution of the hybrid POMs is much more facile in the presence of an excess of the amino acid ligand. Thus the solution studies discussed below have

employed buffer of the corresponding amino acid, in addition to water acidified with HCl. As DMSO proved to be the solvent of choice for voltammetric characterization of the reduced Nle-containing compounds (see later), we also measured solution properties in DMSO for the Nle-analogs only, as the Gly-analogs are insoluble. Instability of the reduced POMs in solution is readily apparent from rapid loss of the blue color, which occurs when the pH of the solution is taken outside the range of around 1.5-4.0. Solutions within this pH range with a POM concentration of greater than 0.2 mM appear to be stable on the order of days, although decomposition and/or further aggregation is apparent after a week in most cases (see later).

Electronic Absorption Spectroscopy. To investigate solution stability in the presence and absence of excess amino acid, electronic absorption spectra in the visible range (Figures 3, S10-S12; Table 3) were measured for the blue reduced compounds **4a**, **4b**, **4c**, **5**, **7a** and **7b** (0.028 mM) in the corresponding amino acid buffer (0.15 Nle or 0.2 M Gly, pH 2.2) and aqueous solution in the absence of excess amino acid (pH adjusted to 2.4 with 3 M HCl prior to dissolution and checked after dissolution). Absorption spectra were also measured in DMSO for the Nle-analogs.

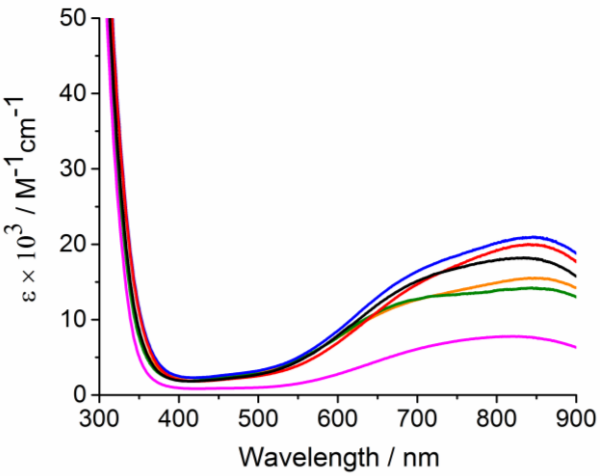

Figure 3. Electronic absorption spectra of 0.028 mM solutions of **4a** (black), **4b** (red), **4c** (blue) **5** (green), **7a** (pink) and **7b** (orange) in 0.15 or 0.2 M corresponding amino acid buffer (pH 2.2)

Table 3. Electronic absorption spectral data for 0.028 mM solutions of reduced compounds **4a**, **4b**, **4c**, **5, 7a** and **7b**

Compound	λ_{max} / nm ($\varepsilon \times 10^3$ / $M^{-1}cm^{-1}$)		
	buffer (pH 2.2)[a]	DMSO	HCl (pH 2.4)[b]
4a	837 (18.1), 715 (sh),	854 (20.1), 702 (sh)	841 (10.3), 706 (sh)
4b	848 (20.0) 734 (sh)	854 (22.4), 701 (sh)	818 (11.3) 734 (sh)
4c	848 (21.0), 734 (sh)	854 (23.6), 715 (sh)	818 (12.6), 732 (sh)
5	843(14.2), 722 (sh)	845 (13.4), 716 (sh)	813(10.6), 713 (sh)
7a	824 (7.7), 707 (sh)	-	804 (6.8), 710 (sh)
7b	853 (15.5), 734 (sh)	-	809 (11.8), 725 (sh)

[a] 0.15 M L-Nle buffer for **4a**, **4b** and **4c**, 0.15 M DL-Nle buffer for **5** and 0.2 M Gly buffer for **7a** and **7b**. [b] unbuffered

The electronic absorption spectra for $\{Mo^{V}_{2}\}$-containing reduced compounds **4a**, **4b**, **4c**, **5** and **7a** and **7b** in buffered and unbuffered aqueous solution and in DMSO all exhibit the strong oxo to metal LMCT bands typical of POMs in the UV region. The visible region in all spectra is dominated by at least two overlapping broad bands between 600 and 900 nm, consistent with the blue coloration, in addition to much weaker bands between 400 and 500 nm. The bands between 600 and 900 nm can be assigned to $Mo^{V} \rightarrow M^{VI}$ (M = Mo, W) IVCT bands that are typical for Mo blues and reduced POMs generally, while Mo^{V} d-d transitions are likely responsible for the weaker bands between 400 and 500 nm. [20,76,85-87] The particular characteristics appear to vary with (i) the solvent medium, (ii) the degree of reduction and (iii) the degree of Mo for W substitution (Figures 3, S7 and S8). Notably for all compounds, spectra measured aqueous solution without excess amino acid are less intense (Figure S7) than those obtained in either buffer or DMSO. The origin of this difference in extinction coefficients is not clear, but the observation points to a decreased stability in the absence of excess amino acid, which is more pronounced for the norleucine analogs than the glycine ones. For the norleucine compounds, the spectra for **5** are all indicative of a lower overall degree of reduction than for **4a**, **4b** and **4c**, which is consistent with results from electrochemical studies (see later). It is interesting to compare the spectra measured for **4a**, **4b** and **4c**, which although of similar degree of reduction, vary in the relative amounts of Mo and W. In buffer, DMSO and water the spectra of compounds **4a**, **4b** and **4c** possess two distinct band maxima at *ca.* 850 and 700 nm, which can be tentatively assigned to $Mo^{V} \rightarrow Mo^{VI}$ and $Mo^{V} \rightarrow W^{VI}$ IVCT transitions, respectively, on the basis of literature studies of mixed-valence mixed Mo/W POMs. [76,85-87] In all solvents, the relative intensities of these two bands are closer for **4a**, while for **4b** and **4c**, the lower energy band is more intense, which might reflect the increase in Mo content from **4a** to **4b** and **4c**.

Regardless of the media, the spectra for Gly-containing **7a** are less intense than those for **4**, **5** and **7b**, while the spectra measured for **7b** are less intense than those for **4**, but more intense than those for **5**. The relative intensities, ie extinction coefficients, of the spectra measured for the different compounds are consistent with the overall decrease in the degree of reduction determined by coulometry (see later): **4b**, **4c** > **7b** > **5** > **7a**, which corresponds to the proportion of 2e-reduced $\{Mo^{V}_{2}\}$-containing versus homovalent M^{VI} (M = Mo, W) POM in each compound.

Change in the absorption spectra over time was investigated for all solutions and found to be strongly dependent on the POM concentration. In all cases, solutions with POM concentrations of at least 0.15 mM all exhibit a loss of signal intensity of less than 15 % after 24 hours (Figure S12), with the stock solution diluted to the measured concentration of 0.028 mM just prior to the measurement. In contrast more dilute 0.028 mM solutions all exhibit a substantially greater loss of signal intensity over 24 hours, which is most pronounced in unbuffered HCl (pH 2.4) without excess amino acid, then amino acid buffer (pH 2.2) and then DMSO. Clearly, as long as the POM concentration is greater than about 0.15 mM and the pH is in the 2.2-2.4 range, the spectra exhibit little change in aqueous buffer solution and in DMSO on a timescale of hours, which is sufficient for the CD, SAXS and electrochemical measurement discussed below. More dilute solutions appear to undergo either oxidation or decomposition of the polyanion.

Small Angle X-ray Scattering (SAXS). Representative oxidized and reduced Nle- and Gly-analogs **3**, **4b** and **7a** were investigated in solution by SAXS to probe the stability of the hybrid POM under different conditions, as well as the sensitivity of the technique to the presence of the aliphatic *n*-butyl chain on the amino acid ligands. The effect of varying both the POM

(0.2-1.2 mM) and amino acid buffer (0.1-1.0 M, pH 2.2) concentration was also explored,-as was the effect of pH variation (pH 0.15-4.0) in unbuffered HCl solution. Samples were measured immediately following dissolution and the data collection time was in the range of 3-9 hours.

The scattering plots of intensity (*I(q)*) versus the scattering vector (*q*), measured for **3**, **4b** and **7a** in amino acid buffer and in unbuffered HCl at pH 2.2, are in reasonable agreement with plots calculated by inputting the solid state single crystal X-ray diffraction data into the SolX program (Figure 4). [65,66] Good linear fits are obtained in the Guinier regime (q = 0.06-0.17 Å^{-1}) for POM concentrations of 0.7 mM or less (Figure S13), while some interaction effects are evident for higher concentrations. The radius of gyration (R_g) is a shape-independent measure of the size of the hybrid POM molecules in solution and R_g values obtained from the Guinier fits are given in Table 4. The R_g values determined for the three different analogs in amino acid buffer are in the range 8.2(4)–9.4(4) Å, in excellent agreement with the values of 8.3-8.6 Å calculated from single crystal data. The scattering plots and R_g values are consistent with maintenance of the solid state structure in solution and show that the solution is monodisperse, i.e. only polyanions of a single size are present. Variation of the hybrid POM concentration (0.2-1.2 mM), the buffer concentration (0.10-0.15M) and pH (1.5-4.0) for **4b** had little effect on the scattering plots or R_g values (Table 4), indicating the general stability of the hybrid POM of **4b** under these defined conditions. However, the SAXS technique is apparently insensitive to the length of the aliphatic chain on the amino acid ligand, with no significant difference between the scattering plots and R_g values measured for the reduced Nle- and Gly-analogs **4b** and **7**. This is most likely due to minimal electron density contrast between the organic ligands and the solvent.

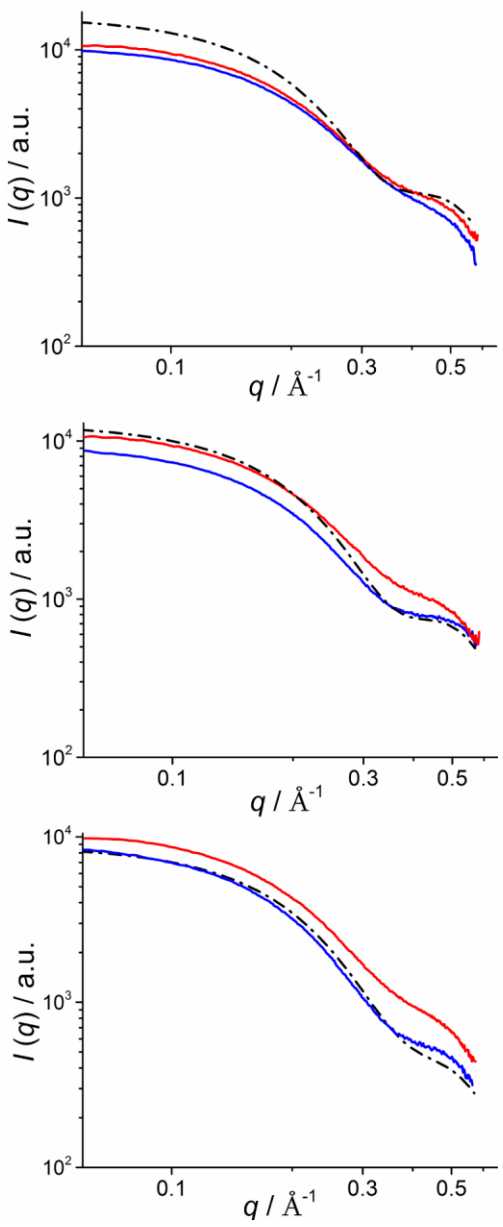

Figure 4. Scattering plots of SAXS data for (top) **3**, (middle) **4b**, and (bottom) **7a** (0.7 mM polyanion) in 0.15 M L-NLe or 0.2 M glycine buffer at pH 2.2 (blue) and unbuffered HCl at pH 2.2 (red). The dashed lines are the curves calculated from the single crystal diffraction data (SolX, normalized to experimental data in buffer)

Table 4. Radius of gyration (*Rg*) values obtained for the hybrid POMs from SAXS studies of **3**, **4b** and **7a** under different conditions

Compound	POM concentration (mM)	Solvent	R_g (Å) [a]	R_g (Å) [b]
3	-	Simulated	8.8 [c]	8.9 [c]
	0.7	L-Nle buffer (0.15 M, pH 2.2)	8.2(4)	8.3(1)
	0.7	HCl (pH 2.2)	8.4(4)	8.2(1)
	0.7	DMSO	5.0(2)	4.5(8)
4b	-	Simulated	8.6 [c]	8.6 [c]
	0.7	L-Nle buffer (0.10 M, pH 2.2)	9.0(4)	
	0.7	L-Nle buffer (0.15 M, pH 2.2)	8.7(4)	8.9(1)
	0.2	HCl (pH 2.2)	8.2(4)	8.2(1)
	0.7	HCl (pH 2.2)	8.5(4)	8.6(1)
	1.2	HCl (pH 2.2)	8.3(4)	8.3(1)
	0.7	HCl (pH 1.5)	8.5(4)	
	0.7	HCl (pH 3.0)	8.5(4)	
	0.7	HCl (pH 4.0)	8.5(4)	
	0.7	DMSO	9.0(4)	9.0(1)
7a	-	Simulated	8.3 [c]	8.4 [c]
	0.7	Gly buffer (0.2 M, pH 2.2)	8.9(4)	9.0(1)
	0.7	Gly buffer (1.0 M, pH 2.2)	9.2(4)	9.4(1)
	0.7	HCl (pH 2.2)	8.5(4)	8.6(1)

[a] From low *q* Guinier fit of SAXS data. [b] From PDDF plots. [c] Simulated from single crystal X-ray diffraction data using SolX program[65,66]

To complement the Guinier plots, which provide a shape-independent measure of the average size, the radial pair distance distribution functions (PDDFs) were determined for all solutions to provide information about the shape of the hybrid POM (Figures S14 and S15). The PDDF is the probability, P(r), that a component of the particle is at a distance, r, from the edge of the particle (r = 0). These were calculated using Moore's method[67] and compared with PDDF curves calculated from the single crystal X-ray diffraction data. In general, reasonable agreement is evident between the measured SAXS data and the plots calculated from the solid state structure for the aqueous solutions of **3**, **4b** and **7a**. Notably, the point at which P(r) goes to zero is in the range 27-33 Å and is consistent with the crystallographically determined diameters of the hybrid POMs. The curves all exhibit two maxima, and in most cases a minor feature at large r, clearly indicating that the hybrid POMs are not spherical. The profile is consistent with the overall shape of the molecules, which all have a low density region in the central core, corresponding to the minimum between the two main peaks – *i.e.* the probably of finding an atom in the center of the hybrid POM is lower than elsewhere. There are subtle differences in the relative heights of the maxima between the SAXS and crystal data. This could be related to particle flexibility in solution compared to in the crystal, as well as the variation in electron density contrast between the solvent and regions of the POM structures under different solution conditions. The R_g values obtained from the PDDF plots (Table 4) are in excellent agreement with the values from the Guinier plots.

Compounds **3** and **4b** were also measured in DMSO (Figure S15), as this was the solvent of choice for electrochemistry (see later). Although the scattering intensity is markedly less than in aqueous solution due to the strong X-ray absorption of DMSO, the scattering plot and PDDF measured for **4b** are in reasonable agreement with the calculated curves. Whilst the poor signal-

to-noise at high q impaired the accuracy of the PDDF fitting procedure, the Guinier fit was unaffected, and the R_g values obtained are consistent with the values obtained in aqueous media (Table 4). This suggests that the hybrid POM of **4b** is stable in DMSO on the timescale of the SAXS measurement. By comparison, the scattering curve measured for **3** is in poor agreement with the calculated curve, and the value of *Rg* determined for **3** in DMSO is significantly smaller than those obtained in aqueous solutions or from simulation. Thus, the oxidized hybrid POM of **3** appears to be unstable in DMSO on the timescale of the SAXS measurement.

On a longer timescale, measurements of **3** and **4b** in buffered and unbuffered aqueous media one week after dissolution reveal changes in the R_g values in all cases. Interestingly, whilst the R_g values decrease in the absence of norleucine buffer, they increase in the presence of buffer, by 10-20 %. The change evident for **3** is greater than for **4b** in both cases. These changes on the longer timescale of a week point to decomposition in the absence of excess Nle but aggregation in the presence of excess norleucine. The latter case perhaps corresponds to the formation of the well-known POM "blackberries" or "vesicles",[88] and is a subject of further ongoing investigation.

Circular Dichrosim (CD) Spectroscopy. Small angle X-ray scattering established the maintenance of the metal-oxo POM framework in buffered solution for the reduced Gly and Nle analogs, but provides no information on whether the amino acid ligands remain coordinated. The presence of electronic transitions in the visible region, and the accessibility of enantiomeric and racemic versions of the reduced Nle-analogs, prompted the use of CD spectroscopy to investigate solution chirality and ligand exchange for some of the (blue) reduced analogs of the present hybrid POMs. A similar CD-based approach allowed the elucidation of the kinetics of ligand exchange of enantiopure thiolate ligands with gold nanoparticles.[89] Spectra were acquired

for representative compounds **4b**, **5** and **7a**, with typical acquisition times of 3 hours and POM concentrations were 0.25 mM. Spectra measured for the L-Nle and D-Nle buffer blanks exhibit the expected Cotton effects in the UV range, but nothing in the visible range, while racemic DL-Nle buffer is CD silent (Figure S16).[90] Spectra measured for L-Nle containing **4b** in L-Nle and D-NLe buffer, HCl (pH 2.4) and DMSO reveal Cotton Effects associated with the electronic absorption transitions in the visible and UV ranges (Figure 5 and Figure S17), indicating maintenance of chirality in solution in each case. The spectra in D-Nle and L-Nle buffer are of opposite sign, suggesting that exchange of the L-Nle ligands with bulk D-Nle from the buffer has occurred on the timescale of the experiment. In contrast, the retention of optical activity apparent from the spectra measured in DMSO and water suggest that the L-Nle ligands remain bound to the hybrid POM in these media and do not exchange rapidly with water or DMSO. Compound **5** possess racemic DL-Nle ligands and no Cotton effects are apparent in racemic DL-Nle buffer solution. However upon dissolution of **5** in L-Nle buffer, the spectrum strongly resembles that of **4b** in the same solution, again suggesting exchange of the racemic Nle ligands for enantiopure L-Nle ligands. Glycine-containing **7a** is achiral in the solid state and in glycine buffer. However the CD spectrum upon dissolution in L-Nle buffer also resembles that of **4b**, indicating that the Gly ligands have been exchanged for L-Nle from the buffer. This amino acid exchange suggested by CD data has been confirmed by the synthesis of **7b** following recrystallization of **4b** from glycine buffer.

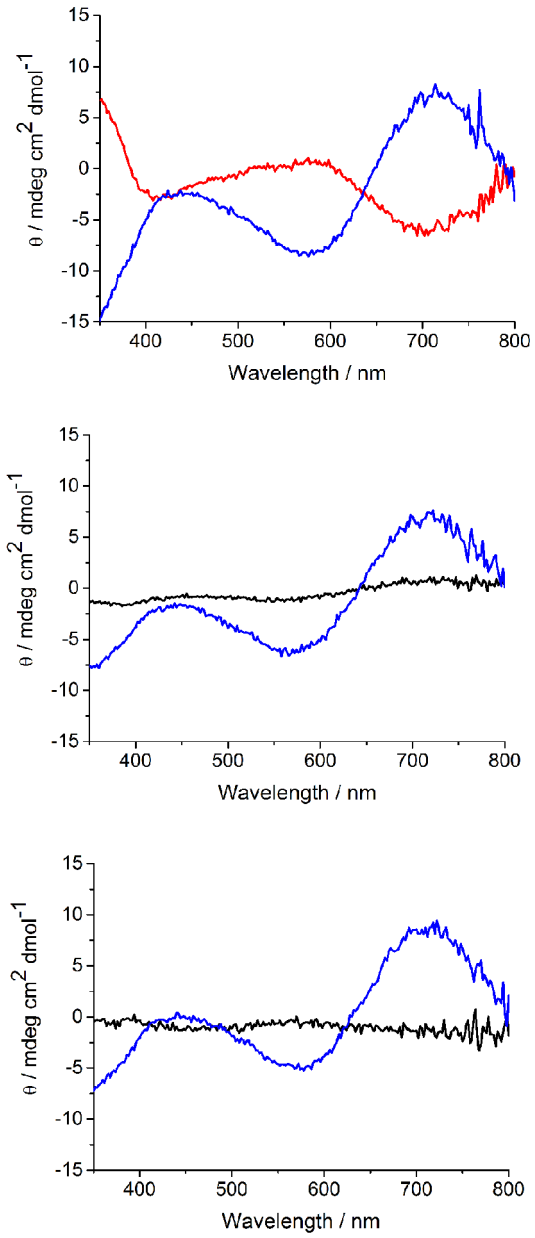

Figure 5. Circular dichroism spectra of (top) 0.25 mM solutions of **4b** in 0.15 M L-Nle buffer (blue), 0.15 M D-Nle buffer (red), (middle) 0.25 mM solutions of **5** in 0.15 M, pH 2.2 DL-Nle (black) and L-Nle (blue) buffer; and (bottom) 0.25 mM solutions of **7a** in 0.2 M, pH 2.2 Gly buffer (black) and 0.15 M, pH 2.2 L-Nle buffer (blue).

The measured CD spectra are all consistent with maintenance of coordinated amino acid ligands for the hybrid POMs in buffered and unbuffered aqueous media in the presence or absence of free amino acid and in DMSO. The data also suggest the exchange of amino acid ligands on the hybrid POMs with other amino acid ligands from buffer, but minimal exchange for water or DMSO ligands. The Cotton Effects are associated with the UV absorption bands of the oxo to metal LMCT bands and with the visible absorption bands assigned as $Mo^{V} \rightarrow Mo^{VI}$ and $Mo^{V} \rightarrow W^{VI}$ IVCT transitions of the reduced POM. Cotton Effects associates with the $V^{IV} \rightarrow Mo^{V}$ IVCT bands of $[PMo_{11}V^{IV}O_{40}]^{5-}$ have been observed previously in the presence of chiral countercations.[50] It should be noted that the POM backbone of the present compounds is achiral in the absence of any amino acid ligands due to the approximate C_{2v} point symmetry. This is in contrast to literature examples where chiral tartrate or proline ligands enhance chirality in hybrid zirconium or lanthanoid phospho- and silico-tungstates. [52-54] In the literature studies the POMs themselves are chiral and the effect is an overall enhancement of chirality by incorporation of chiral organic moieties, with each enantiomer of the organic species selectively binding to, or associating with, one enantiomeric form of the chiral POM.

NMR Spectroscopy. The synthesis of Gly-containing **7b** from Nle-containing **4b** and the CD results discussed above confirm the possibility of exchanging of amino acid ligands in this structural family of hybrid POMs, while retaining the POM framework. Previous studies of hybrid POMs incorporating carboxylate and other ligands have demonstrated the utility of ^{1}H NMR spectroscopy for studying ligand exchange in solution. In particular, 1D ^{1}H NMR spectra of the carboxylate-ligated Keplerate POMs exhibit distinct resonances for bound and unbound carboxylate ligands.[91-93]

Room temperature ^{1}H NMR spectra of Nle-containing oxidized **3** and reduced **4b** in D_2O are very similar (Figure S18) and the spectra remain unchanged on the timescale of days to weeks. Distinct resonances are evident for each of the *p*-$MeBzNH_3^+$ and Nle/$NleH^+$ protons with chemical shift values very close to those of free Nle and *p*-$MeBzNH_2$. The integration values of these resonances are important for establishing the overall formulations of the compounds, in conjunction with crystallography and elemental analysis data. The peaks in the ^{1}H NMR spectrum of **3** are sharp, the multiplicities due to coupling are evident and there is no sign of paramagnetic broadening or shifting. The resonances measured for both the *p*-$MeBzNH_3^+$ and Nle/$NleH^+$ moieties of **4b** occur at the same chemical shifts as those for **3**, however the peaks attributed to the amino acid protons are somewhat broadened and a second set of very broad, lower intensity resonances are evident, shifted downfield. This second set of broader resonances integrates to approximately 30 % of the main set and clearly indicates more than one environment for the Nle/$NleH^+$ moieties. Close inspection of the spectrum for **3** also reveals a similar additional set of resonances, although they are of much lower intensity for **3**. Addition of free L-Nle to the solutions does not give rise to a set of distinct resonances for free Nle/$NleH^+$, instead increasing the intensity of the observed set of Nle/$NleH^+$ peaks. This is consistent with previous studies of the $[XMo_6O_{21}(AA)]^{n-}$ (X = Se^{IV}, Sb^{III}, Bi^{III}; AA = L-lysine or L-alanine) family, in which addition of free amino acid did not afford a separate set of for the amino acid protons.[51] This was attributed to either rapid ligand exchange or an insignificant chemical shift difference due to the minimum of four bonds separating the metal centers and amino acid protons. In order to probe the possibility of chemical exchange between free and bound Nle, variable temperature spectra were measured for **3** in the temperature range 25-70 °C (Figure S19). All of the peaks due to the *p*-$MeBzNH_3^+$ cations and Nle/$NleH^+$ shift monotonically

downfield with temperature, with no sign of decoalescence of exchanging protons. These observations indicate that exchange between free and bound Nle/NleH$^+$ must be fast on the ^{1}H NMR timescale at room temperature and above. No broadening is evident for the peaks corresponding to the *p*-MeBzNH$_3^+$ cations in the variable temperature experiment. In contrast, the peaks associated with the Nle protons broaden upon heating and the extent of broadening appears to inversely correlate with the number of bonds from the Nle carboxylate group, with peak due to the methine protons (δ = 3.85 ppm at 25 °C) broadening most significantly. This may be ascribed to the effect of segmental motion along the carboxylate-tethered aliphatic *n*-butyl sidechain of the Nle ligands and the temperature-induced increased rate of tumbling of the macromolecular hybrid POM.[94,95] Variable temperature ^{1}H NMR spectra measured for **4b** were similar to those measured for **3**, notably the additional lower intensity broad set of resonances associated with the Nle/NleH$^+$ protons shifts as per the higher intensity, sharper set, but they do not broaden and the two sets did not coalesce (Figure S20).

The ^{13}C{^{1}H} NMR spectra of **3** and **4b** in D_2O (Figures S21and S22), acquired overnight on a high resolution 800 MHz spectrometer on nearly saturated samples, shows the resonances for the *p*-MeBzNH$_3^+$ cations and Nle/NleH$^+$ moieties at the typical chemical shifts values. As per the ^{1}H NMR spectrum, there are an additional lower intensity set of resonances associated with the Nle/NleH$^+$ resonances, which are downfield from the main peaks and more intense for **4b** than **3**. To ascertain whether additional sets of ^{1}H and ^{13}C resonances are correlated, a 2D ^{1}H-^{13}C heteronuclear single quantum coherence (HSQC) spectrum was also collected for **4b** in D_2O (Figures S23 and S24). In addition to the expected single crosspeak for each of the the *p*-MeBzNH$_3^+$ cation C atoms, the HSQC spectrum exhibits crosspeaks between the major and minor sets of resonances associated with the Nle/NleH$^+$ moieties, such the major set of ^{1}H and

^{13}C resonances correlate with each other, as do the minor set of ^{1}H and ^{13}C. Overall, this spectrum suggests up to four different Nle/NleH^{+} environments (Figure S24). These are most obvious for the α-C(H) and β-C(H$_2$) groups, which exhibit three and four clear sets of crosspeaks, respectively. In addition to three distinct types of bound Nle ligand (two bidentate and one monodentate, Figure S3), free NleH^{+} countercations as well as free Nle zwitterions may exist in solution, which can account for the multiple observed species. The effect of the different environments on the chemical shifts should correlate with the distance from the amine and carboxylate groups, consistent with the observation of the largest effect for the α-C(H) and β-C(H$_2$) groups. Indeed the chemical shift difference for the carboxylate C atom is consistent with the results from ^{13}C NMR studies of carboxylate-ligated metal complexes with carboxylate ligands bound in different modes.[96 97] The relatively higher intensities of the additional resonances for **4b** versus **3** is consistent with the absence from **3** of the monodentate Nle ligand and free zwitterionic norleucine that are present in **4b**.

Although ^{89}Y, ^{95}Mo and ^{183}W NMR have both been useful for determination of POM solution structure,[36,37] for the present compounds the solubilities and symmetry are too low for these techniques to be useful.

Electrochemistry. Having established with SAXS and CD spectroscopy the solution stability of the reduced hybrid Gly and Nle POMs in certain media, voltammetric and coulometric studies were undertaken to determine the degree of reduction and explore the possibility of interconverting between the oxidized and reduced analogs. Electrochemical studies of the {Mo$^{V}_2$}-containing reduced Nle-containing species **4a**, **4b**, **4c** and **5** were performed in DMSO (0.05 M Bu$_4$NPF$_6$), due to the strong adsorption of the complexes on the electrode surface in aqueous media (Figures 6, S25 and S26). Small angle X-ray scattering

suggests that oxidized analog **3** is unstable in DMSO, which prevents comparison of electrochemical data. Transient cyclic voltammograms for all the chemically reduced analogs **4a**, **4b**, **4c** and **5** show an irreversible oxidative process at all the scan rates (0.05 to 1 V s^{-1}) studied, with a peak potential, E_p, of around -0.19 V at a scan rate, ν, of 100 mV s^{-1}. All compounds exhibit at least two irreversible reductive processes at potentials more negative than -0.5 V, which could be assigned to the reduction of the W or Mo centers. Details of these reduction processes are not discussed here as they are beyond the focus of this study. The near steady-state mass transport limiting currents associated with the oxidative process for compounds **4a**, **4b** and **4c** are similar after the concentrations are taken into account, suggesting similar degrees of reduction. In addition, the limiting current of the oxidative process is less than half of that of the first reductive process. After exhaustive oxidative electrolysis of **4b** and **4c** at –0.01 V, the solution changed from dark blue to colorless, and no oxidation process was observed in both cyclic and RDE voltammograms, confirming complete oxidation of all Mo^{V} to Mo^{VI}. The charge consumed during the oxidative electrolysis is consistent with oxidation by 1.8(2) electrons per polyanion for both compounds. The voltammograms obtained after electrolysis do not exhibit a reductive process at a potential similar to the oxidative process in the parent compound, indicating that it is not possible to electrochemically interconvert between $\{Mo^{V}_2\}$-containing **4b** and **4c** and a homovalent analog with a $\{Mo^{VI}_3W^{VI}\}$ core, which is consistent with the irreversible nature of the process observed from voltammetry. Exhaustive oxidative electrolysis of **5** at –0.01 V again converts the solution from dark blue to colorless, with the disappearance of the oxidation process in both cyclic and RDE voltammograms measured after the electrolysis, confirming complete oxidation of all Mo^{V} to Mo^{VI}. The charge passed is consistent with oxidation by 1.3(2) electrons per polyanion. The different numbers of electrons measured by

coulometry of **4b** and **4c** versus **5** is consistent with the extinction coefficients from the electronic absorption spectra (see above) and the composition of **5** involving a smaller proportion of 2e-reduced polyanions than **4b** and **4c**.

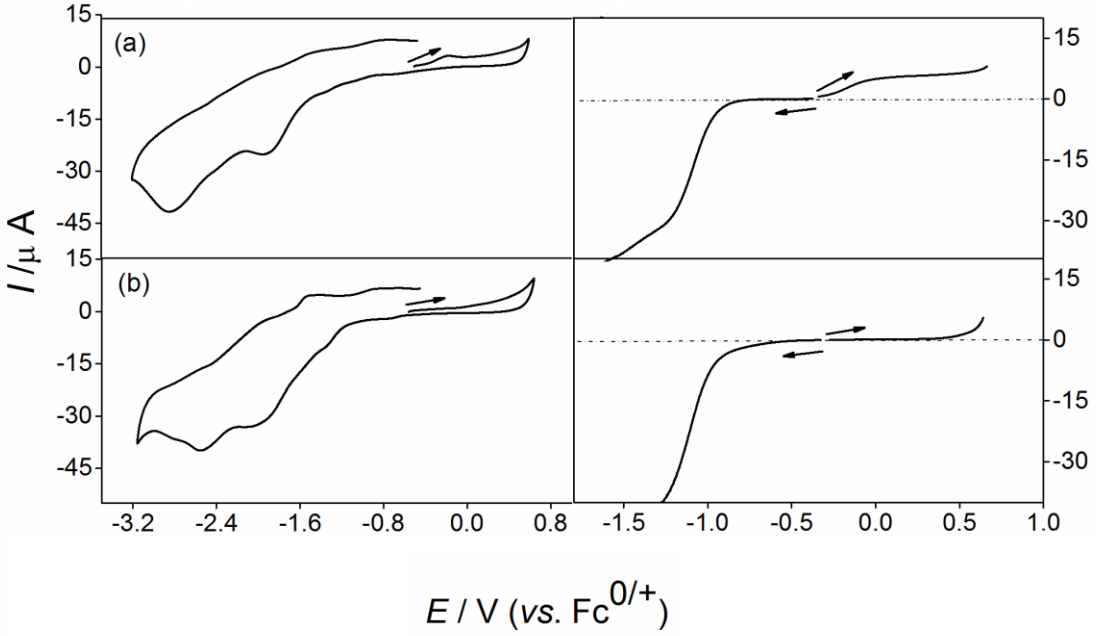

Figure 6. Cyclic (left) and RDE (right) voltammograms of Nle-containing compounds (a) **4b**, (b) **4b** following oxidative electrolysis, for CV ν = 100 mV s^{-1} and for RDE ν = 20 mV s^{-1} and ω = 104.7 rad s^{-1}.

Transient cyclic and steady state rotating disk electrode (RDE) voltammograms (Figure 7) were also measured on freshly prepared solutions of Gly-containing compounds **6**, **7a** and **7b** (0.3 mM polyanion, in 0.2 M Gly buffer, pH 2.2). These compounds were measured in aqueous solution in contrast to the DMSO employed for the Nle-analogs because they are insoluble in DMSO and no electrode adsorption problems are apparent. Again $\{Mo^{V}_{2}\}$-containing reduced analogs **7a** and **7b** exhibit an irreversible oxidative process at all scan rates (0.05 to 1 V s^{-1}) studied, with an E_p of +0.54 V at ν of 100 mV s^{-1}, while no equivalent reductive process was

observed for the oxidized analog **6**. The magnitude of the steady-state mass transport limiting current associated with the oxidative process for **7a** is approximately half of that for **7b**, indicating that **7b** is comprised of a significantly larger proportion of 2e-reduced $\{Mo^{V}_{2}\}$-containing POM. As for the Nle-containing species, exhaustive electrolysis of **7a** and **7b** at +0.6 V again converts the solutions from dark blue to colorless, with the close to zero current measured in the positive potential range in the RDE voltammogram after the electrolysis confirming complete oxidation. The charge passed indicates oxidation by 0.7(2) and 1.5(2) electrons per polyanion for **7a** and **7b**, respectively, as the fraction of 2e-reduced, $\{Mo^{V}_{2}\}$-containing POM in each compound is oxidized. The lesser degree of reduction apparent for **7a** versus **7b** from the RDE limiting currents and coulometry is consistent with the electronic absorption spectra (see above). Neither **6**, nor electrochemically oxidized **7a** or **7b**, exhibits a reduction process in the potential range similar to the oxidation process of **7a**, suggesting that electrochemical interconversion of these hybrid POMs is not possible, as per the norleucine analogs

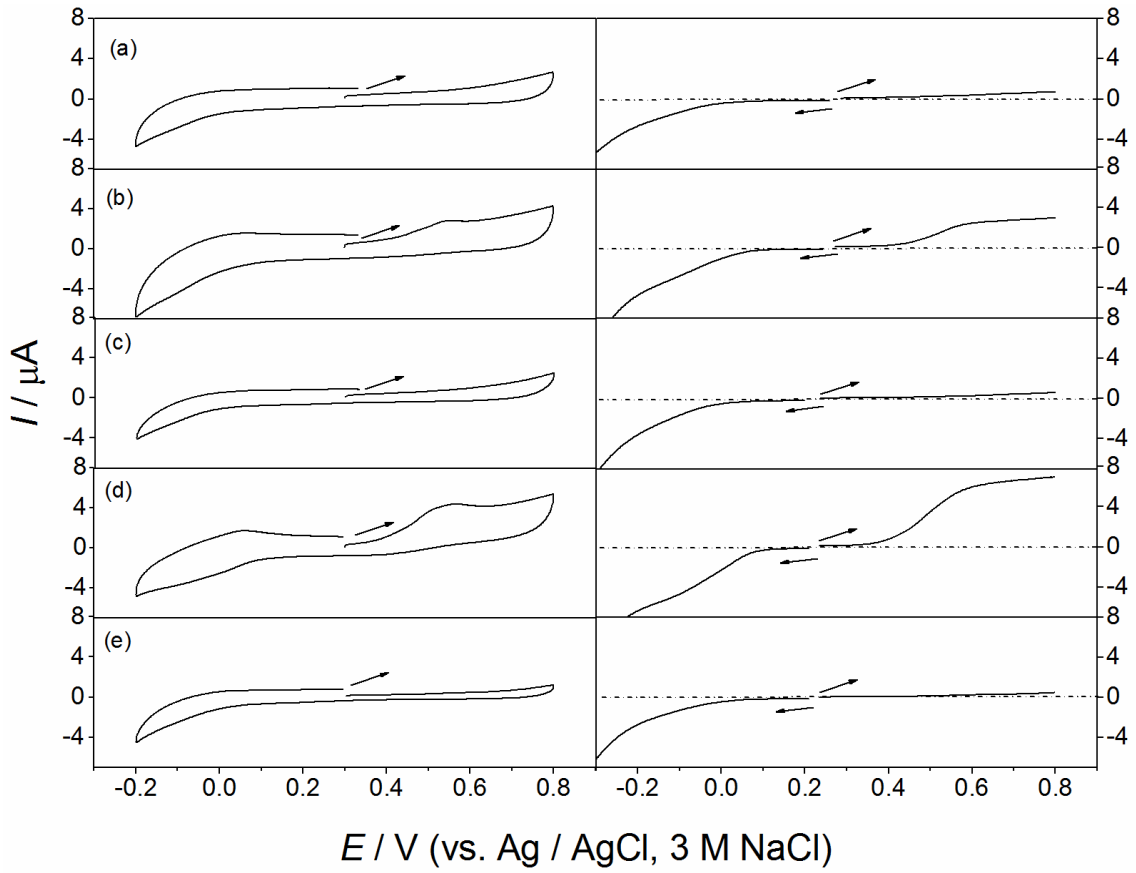

Figure 7. Cyclic (left) and RDE (right) voltammograms of 0.3 mM Gly-containing compounds (a) **6**, (b) **7a** (c) **7a** following oxidative electrolysis, (d) **7b** and (e) **7b** following oxidative electrolysis, in 0.2 M Gly buffer, pH 2.2; for CV ν = 100 mV s^{-1} and for RDE ν = 20 mV s^{-1} and ω = 104.7 rad s^{-1}.

Density Functional Theory (DFT) Calculations. Density Functional Theory calculations were employed to probe the trends observed experimentally concerning the relative stabilities of the different hybrid POM analogs and positional isomers, and the facility of their reduction. To save computational time, simplified model compounds with no terminal aqua ligands and formate ligands instead of amino acid ligands were employed for all calculations.

Complexes with a trimetallic core were thus modelled as $[As_4(M^{VI}_3)M^{VI}_{44}Y_4O_{159}(O_2CH)_8]^{20-}$ (M = Mo, W, abbreviated as $\{Mo_3\}Mo_xW_{44-x}$ and $\{W_3\}Mo_xW_{44-x}$), while those with a tetrametallic core were modelled as $[As_4(M^{VI}_4)M^{VI}_{44}Y_4O_{160}(O_2CH)_8]^{16-}$ (abbreviated as $\{Mo_yW_{4-y}\}W_{44}$ and $\{Mo_yW_{4-y}\}Mo_xW_{44-x}$).

$\{Mo_3\}Mo_xW_{44-x}$ compounds. Crystallographic data (see above) for all characterized compounds indicate a very marked preference for location of Mo atoms in the internal tri- or tetrametallic core, over all other structural sites (Table 2, Figure S2). Calculations are consistent with this observation, with total binding energy values for the pair of positional isomers $\{Mo_3\}W_{44}$ and the hypothetical $\{W_3\}Mo_3W_{41}$ confirming that the former is the most stable by 14.7 kcal mol^{-1} (Table S2). Thus, on average, each Mo center in a core site is *ca*. 5 kcal mol^{-1} more stable than in a "non-core" site. The origin for this trend is unclear, although is likely related to subtle differences in the radii of $Mo^{V/VI}$ and $W^{V/VI}$ versus the size of the internal metal-oxo core defined by the external POM framework.

The preference for localization of the Mo atoms in the central core above all other sites is very clear. However, all of the crystallographically characterized compounds described above also possess between 0.5 and 2.5 additional Mo atoms disordered with W atoms in the external non-core POM framework, with a further preference for localization of Mo in the $\{Y_4M_8L_8\}$ "ring" and $\{AsM_9\}$ "triad" sites over the $\{AsM_9\}$ "belt" (Figure S2). Several different positional isomers of the $\{Mo_3\}Mo_xW_{44-x}$ (x = 0–3) series were calculated to explore this aspect, with the Mo atoms occupying different sites. The calculated binding energies and interatomic parameters are reported in Tables S2 and S3, respectively. In general, all of the optimized $\{Mo_3\}Mo_xW_{44-x}$ structures exhibit longer interatomic distances and wider bond angles than are apparent from the single crystal structural data for homologous **3w** (Table 2), with the exception of the terminal

M=O distance. This fact suggests that the optimized geometry is naturally *expanded* with respect to the crystal structure. This is a well-known tendency in solution, which is the approach taken to compute the optimized structures via a continuum solvent model. Another source of discrepancy between the crystallographic and computed structures is that the experimental interatomic distances of the internal square core are averaged over the four sites, including the vacancy. It is worth mentioning that the computed M-O(-M) distances show a wide range of values, reminiscent of the Mo-O-Mo *alternating bond length* feature characteristic of polyoxomolybdates,[98] which are not apparent in the crystallographic data due to the effect of averaging over the equivalent sites.

The frontier orbital energies of the $\{Mo_3\}Mo_xW_{44-x}$ series and the difference in total binding energy between the positional isomers with the same x value are presented in Figure 8, along with frontier orbital energies for two members of the hypothetical $\{W_3\}Mo_xW_{44-x}$ series, for comparison. For x = 1, the form with the external Mo located in a $\{AsM_9\}$ triad is 3.8 kcal mol^{-1} more stable than that with Mo in the $\{Y_4M_8L_8\}$ ring. For x = 2, $\{Mo_3\}Mo(ring)Mo(triad)W_{42}$ is 5 kcal mol^{-1} more stable than $Mo(ring)_2W_{42}$. For the hypothetical 2e-reduced forms of $\{Mo_3\}Mo_xW_{44-x}$ with x = 1 and 2 we compute ΔE = 2.1 kcal mol^{-1} and 0.073 kcal mol^{-1}, respectively. This latter trend is consistent with the Lowest Unoccupied Molecular Orbitals (LUMOs) of the least stable oxidized forms. For x = 3, $\{Mo_3\}Mo_2(ring)Mo(triad)W_{41}$ is estimated to be 6.0 kcal mol^{-1} less stable than $\{Mo_3\}Mo(ring)Mo_2(triad)W_{41}$. Thus, for all $\{Mo_3\}Mo_xW_{44-x}$ compounds with $x > 0$, the external Mo centers exhibit a thermodynamical preference for the triad positions of $\{AsM_9\}$ over the $\{Y_4M_8L_8\}$ ring positions in all cases calculated. However, this contrasts with the crystallographic

analysis, namely the higher Mo occupancy of ring positions compared with triad positions, a fact likely ascribed to kinetic rather than thermodynamic control during synthesis and crystallization.

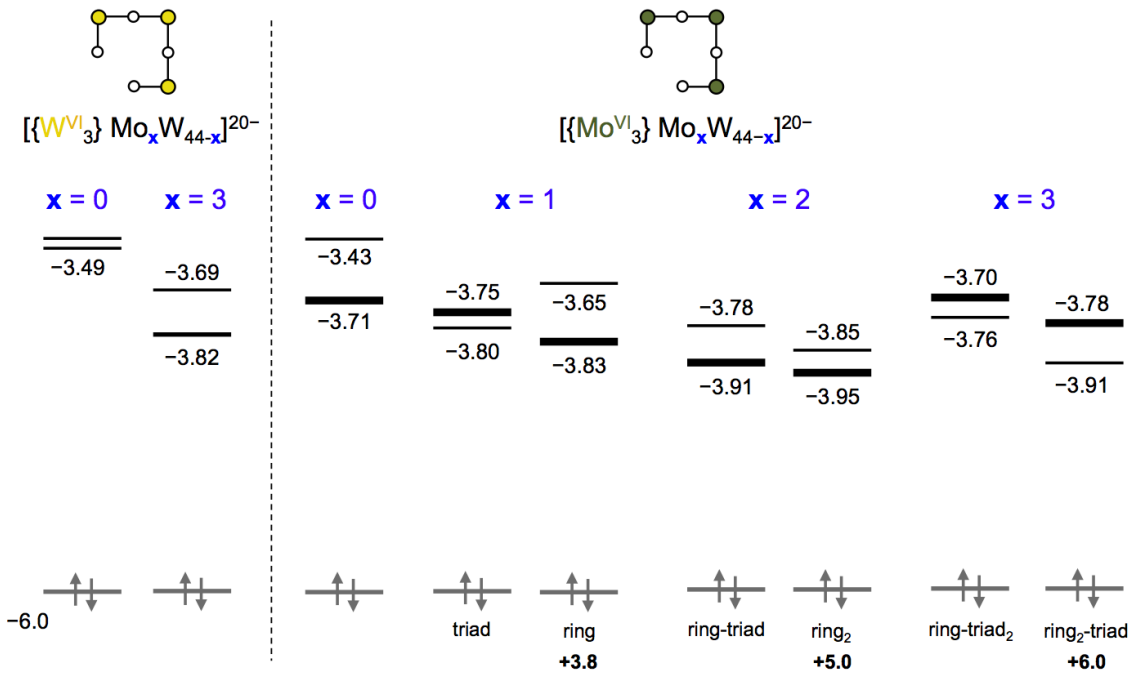

Figure 8. Electronic structure of fully oxidized $[\{W_3\}Mo_xW_{44-x}]^{20-}$ (x = 0 and 3) and $[\{Mo_3\}Mo_xW_{44-x}]^{20-}$ (x = 0–3) systems in aqueous solution. The HOMO (grey), LUMO and LUMO+1 energies (in eV) are shown, with thick lines representing orbitals localized on the $\{Mo_3\}$ core (see Figure S14). Below the HOMOs, the localization (triad or ring) of the x external Mo atoms is indicated, together with the binding energy differences (kcal mol^{-1}) between compounds with the same x value.

In Figure 8, the fully oxidized $\{Mo_3\}Mo_xW_{44-x}$ and $\{W_3\}Mo_xW_{44-x}$ compounds (charge: q = –20) feature Highest Occupied Molecular Orbitals (HOMOs) at a constant energy of –6.0 eV, irrespective of the composition of the external Mo_xW_{44-x} framework. That is, the number of Mo centers in the external framework does not affect the energies of the HOMOs. The LUMOs

feature a slow tendency to stabilize as the composition of the external "non-core" framework of $\{Mo_3\}Mo_xW_{44-x}$ becomes richer in Mo (x varying from 0 to 3), which is also apparent for the two hypothetical $\{W_3\}Mo_xW_{44-x}$ species (x = 0 and 3). This trend follows the evidences reported for other mixed-metal POMs, for which LUMO energies typically decrease (concomitantly increasing the oxidizing power) as the Mo/W ratio increases.[99] Taking $\{Mo_3\}W_{44}$ as reference, the LUMO at –3.7 eV is fully localized on the internal Mo-based trinuclear core (Figure S27). Increasing the number of non-core Mo centers in $\{Mo_3\}Mo_xW_{44-x}$ changes the nature of the lowest energy metal-based orbitals. As the LUMO associated with $\{Mo_3\}$ is rather high in energy, the presence of non-core Mo atoms can vary the localization of the LUMO. Calculations suggest this is the case for $\{Mo_3\}$Mo(triad)W_{43} and $\{Mo_3\}$Mo(ring)Mo(triad)$_2W_{41}$ (Figure S27), for which the LUMOs are located on Mo centers in the peripheral $\{AsM_9\}$ units of the POM framework. This is not the case for the $\{Mo_3\}$Mo(ring)W_{43} or $\{Mo_3\}Mo_2W_{42}$ systems, for which the LUMO remains localized on the trinuclear core.

Comparison of $\{Mo_3\}$ and $\{Mo_yW_{4-y}\}$ cores. In this work, we have modelled the hybrid POM structures containing an internal trimetallic $\{Mo_3\}$ core, which are compared with analogous calculations recently communicated by some of us for analogs with tetrametallic $\{Mo_yW_{4-y}\}$ cores.[55] Recalling these theoretical results, we observe that the number of core Mo atoms (y) strongly affects the electronic affinity and reducibility of the POM. From $\{W_4\}$ to $\{Mo_4\}$, the absolute energies of the LUMOs gradually decrease in energy by 0.7 eV in total (Figure 9). Thus, we concluded that the $\{Mo_4\}$ and $\{Mo_3W\}$ species are readily reduced and accommodate two (paired) electrons in the internal core. The reduced $\{Mo^{V}_2W^{VI}_2\}$ species is likely also accessible. On the other hand, the calculations indicate that species with $\{Mo_yW_{4-y}\}$ (y < 2) cores are considerably more difficult to reduce and we have no experimental evidence for

the formation of these analogs. It must be noted that for all $\{Mo_yW_{4-y}\}Mo_xW_{44-x}$ species, the Mo/W composition of the non-core POM framework does not affect the redox state of the POM or its ease of reduction. This is due to the comparatively high energy of the first empty orbital that is localized on the non-core part of the POM framework. These theoretical results are in good agreement with the present experimental findings regarding the facility of reduction of the analogs with a tetrametallic core.

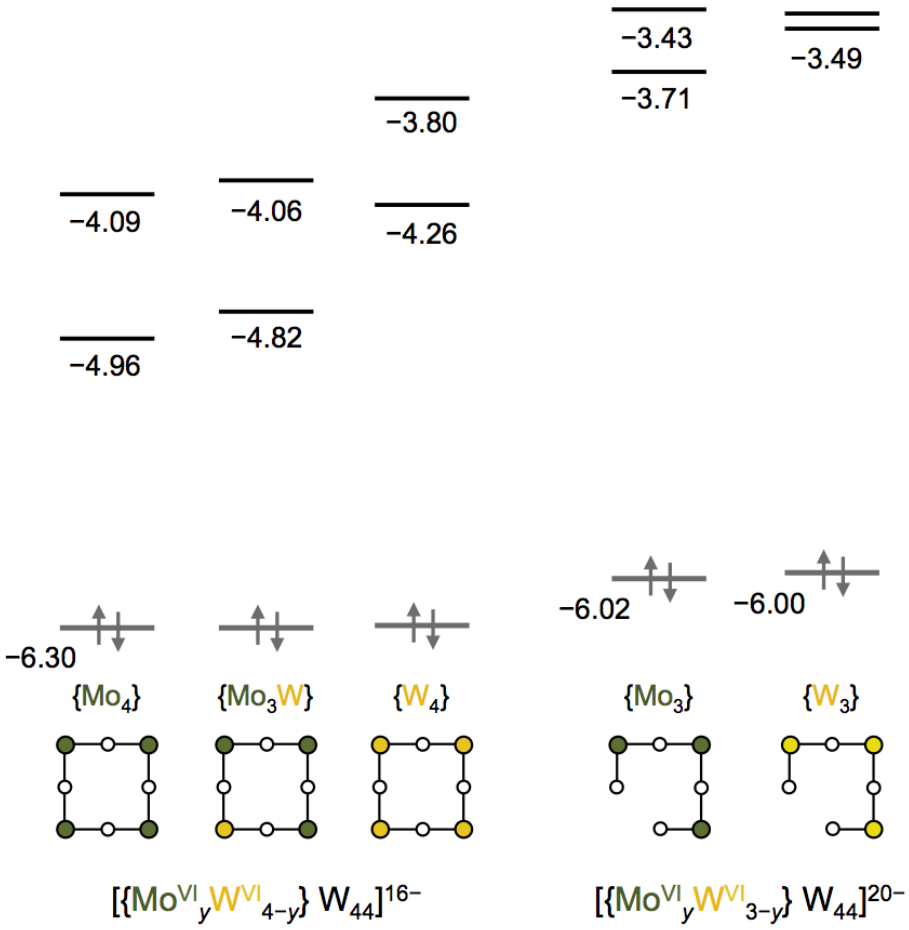

Figure 9. Frontier molecular orbital energies (eV) computed for the structures indicated. The internal $\{M_4\}$ or $\{M_3\}$ core is shown schematically (color code: W, yellow; Mo, green; O, white).

Let us now compare the formally fully oxidized (hexavalent Mo^{VI}/W^{VI}) $\{Mo_3\}W_{44}$ and $\{W_3\}W_{44}$ species with $\{Mo_4\}W_{44}$ structures in aqueous solution (the optimized DFT geometries of $\{Mo_3\}W_{44}$ and $\{Mo_4\}W_{44}$ can be found in Table S4). The LUMO and HOMO are found at –3.71 and –6.02 eV for $\{Mo_3\}W_{44}$, whereas the values are –3.49 and –6.00 eV for $\{W_3\}W_{44}$ (Figure 8). For $\{Mo_3\}W_{44}$ the LUMO and LUMO+1 are localized on the internal trinuclear core (Figure 10), at variance with hypothetical compounds based on the $\{W_3\}$ internal moiety (see LUMO and LUMO+1 in Figure S28, left). In the $\{Mo_yW_{4-y}\}W_{44}$ systems, with the tetranuclear core (q = –16) the homologous orbitals are found at –4.26/–6.30 eV for $\{W_4\}W_{44}$, at –4.82/–6.30 eV for $\{Mo_3W\}W_{44}$ and at –4.96/–6.30 eV for $\{Mo_4\}W_{44}$. In all cases, the HOMO is located on the $\{AsO_3\}$ heteroatomic groups of the peripheral lacunary Keggin moieties and the LUMO is localized on the internal metal-oxo square core. From $\{Mo_yW_{4-y}\}W_{44}$ to $\{Mo_3\}W_{44}$, the energy change in the HOMO is minor (0.27 eV), whereas the LUMO of $\{Mo_3\}W_{44}$ is 1.25 eV higher than that of $\{W_4\}W_{44}$, which is the highest of all species with a tetranuclear core. The change in the HOMO energy arises mainly from the molecular charge variation and it is modest due to the relatively high nuclearity of the system, which largely dissipates the charge effect. On the other hand, removal of one metal center from the internal square core has dramatic consequences on the LUMOs, which are localized in the internal core as well. Accepting that the pure charge effect applies similarly to the occupied and unoccupied orbitals, the larger energy change for the unoccupied orbitals must originate from the effect of the "broken" or incomplete internal loop,

because of the missing $\{MO\}^{4+}$ unit. Thus, the extra stability of the associated LUMOs conferred by the closed $\{Mo_yW_{4-y}\}$ metal-oxo loop is absent for the $\{Mo_3\}Mo_xW_{44-x}$ series with the trinuclear core. A similar stabilizing effect of closed metal-oxo rings has been previously reported by some of us for other POMs.[100] The main effect of loop-opening is a large increase in energy for the MOs localized on the internal core, which includes the orbitals that will accept electrons upon reduction. These theoretical results explain why the $\{Mo_3\}Mo_xW_{44-x}$ family is intrinsically more difficult to reduce (ie accommodate metal-based electrons) than any $\{Mo_yW_{4-y}\}Mo_xW_{44-x}$ analog. This is consistent with the experimental observation that the compounds with the trinuclear $\{Mo_3\}$ core are invariably obtained in the oxidized hexavalent (Mo^{VI}/W^{VI}) form under ambient conditions, while the analogs with the tetranuclear form are prone to reduction. For comparison purposes, the $[PW_{12}O_{40}]^{3-}$ Keggin and $[P_2W_{18}O_{62}]^{6-}$ Wells-Dawson anions, two well-known POMs that are readily reduced, have LUMOs around –4.4 eV in aqueous solution,[101] that is, as much as 0.7 eV lower than $\{Mo_3\}W_{44}$. From the point of view of molecular stability, we suggest that non-reducible POMs, such as the $\{Mo_3\}$-containing species **3** and **6**, are less stable than the readily reduced $\{Mo_yW_{4-y}\}$-containing ones, such as **4**, **5** and **7**.

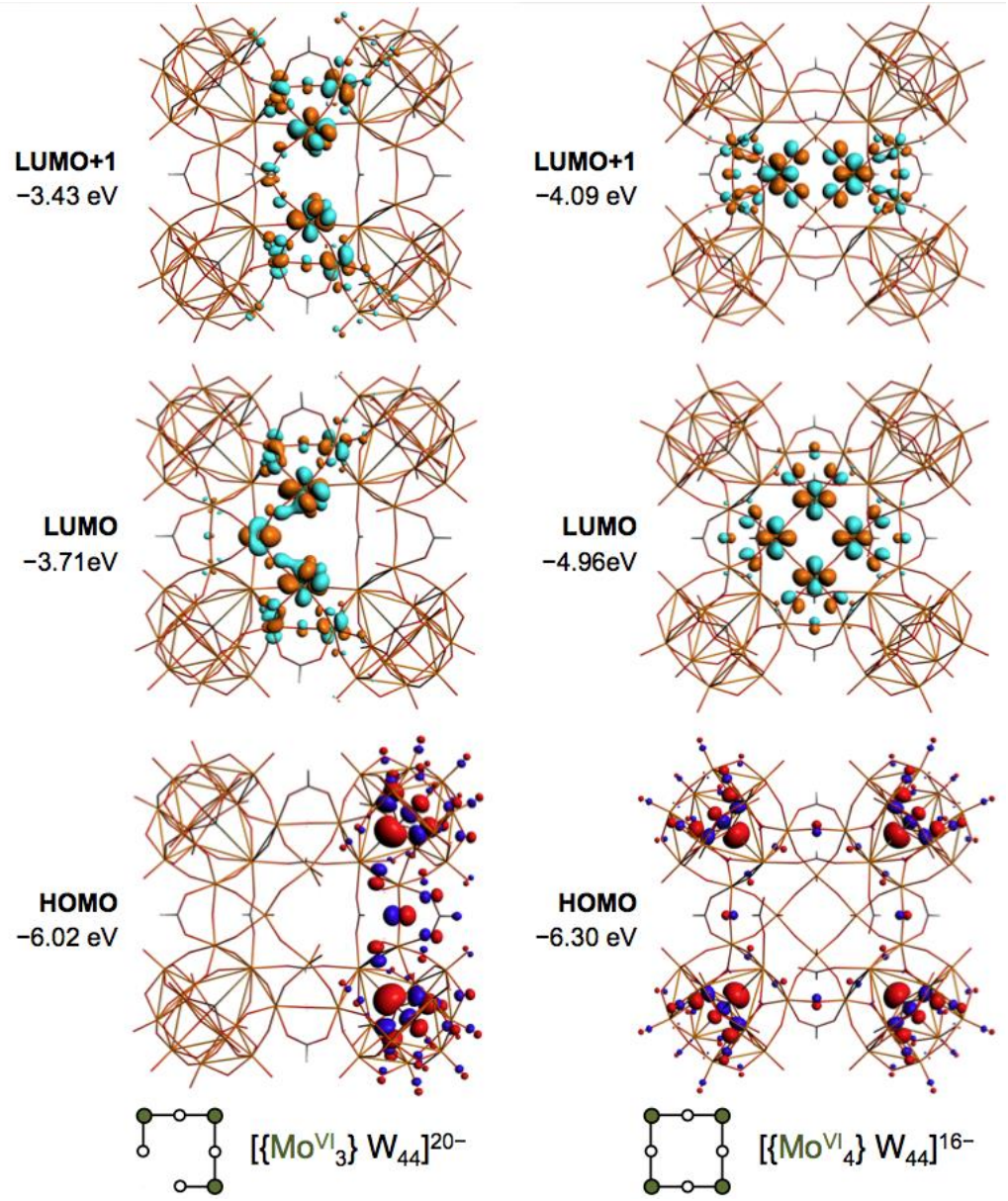

Figure 10. Frontier orbitals (3D representation and energy) computed for fully oxidized $\{Mo_3\}W_{44}$ (q = –20) and $\{Mo_4\}W_{44}$ (q = –16). Although the orbitals are similarly localized and have the same nature in both compounds, the different molecular charge and the open/closed arrangement of the internal loop afford the large energy differences (in eV) notably for LUMOs and LUMO+1s.

The reduced compounds **4, 5** and **7** discussed herein are formulated as being partially (**5** and **7**) or fully (**4**) comprised of a tetranuclear 2e-reduced species, formulated as $\{Mo^{V}_{2}Mo^{VI}W\}$. As discussed above, the available experimental data does not allow us to distinguish between a single POM with a $\{Mo^{V}_{2}Mo^{VI}W\}$ core, or an equal mixture of POMs with $\{Mo^{V}_{2}Mo^{VI}_{2}\}$ and $\{Mo^{V}_{2}W^{VI}_{2}\}$ cores. We have computed the 2e-reduction reaction energies for the corresponding fully oxidized, hexavalent species corresponding to both cases and found an energy difference of only 1 kcal mol^{-1}, in favour of the 50:50 mixture of species with $\{Mo^{V}_{2}Mo^{VI}_{2}\}$ and $\{Mo^{V}_{2}W^{VI}_{2}\}$ cores. However the modest size of this energy difference is insufficient to provide full clarification of this point.

Concluding Remarks

A comprehensive investigation of various members of a family of heterometallic POMs with amino acid ligands indicates a robust POM framework that is readily modified in terms of the nuclearity of the metal-oxo core, the metal composition, the redox state and the amino acid ligands. In the absence of visible light or a chemical reductant, the reaction product is the fully oxidized homovalent Mo^{VI}/W^{VI}-containing hybrid POM with a trinuclear $\{Mo^{VI}_{3}\}$ core, while light-induced or chemical reduction affords species with a tetrametallic core, with varying proportions of an overall 2e-reduced species with a $\{Mo^{V}_{2}M^{VI}_{2}\}$ core (M = Mo or W) mixed with the oxidized hexavalent analog. The reduced compounds exhibit the dark blue color characteristic of classical "heteropoly blues" and are diamagnetic with the two additional electrons strongly antiferromagnetically coupled. These reduced compounds are air stable in the solid state; they can be oxidized in solution, but this process is irreversible; the oxidized analog

is unstable and attempts to re-reduce the oxidized solution are unsuccessful. This behavior is reminiscent of the Mo-blue giant wheels, the fully oxidized Mo^{VI} analogs of which are not accessible. In contrast to the analogs with a tetrametallic core, those with a trimetallic $\{M_3\}$ core are not readily reduced; they are not photoreduced in the solid state and in solution they do not exhibit a reductive electrochemical process at an accessible potential that corresponds to a simple reduction to the 2e-reduced analog. This is consistent with DFT calculations that indicate that the LUMO is much higher in energy for analogs with the $\{M_3\}$ versus $\{M_4\}$ core. For the complexes with the tetrametallic core, the $\{M_4\}$ closed loop confers extra stability on the LUMO associated with this moiety, resulting in facile 2e-reduction and accommodation of the two electrons in this MO. This reduction is so facile that a fully oxidized analog with a hexavalent tetrametallic core cannot be isolated. In contrast, the $\{M_3\}$ open loop affords much higher energies for the LUMO and LUMO+1, with no apparent reduction evident for complexes with the trimetallic core. This observation is analogous to linear and ring-conjugated pi-systems, where the orbital energies of the pi-system are lower in rings, i.e. aromatic molecules. Thus, despite the similarity of their structures, the oxidized and 2e-reduced analogs of these hybrid POMs cannot be readily interconverted, due to the different numbers of metal centers in the core metal-oxo units of the POMs which result in difficult to reduce $\{M_3\}$ open loops versus easily reduced $\{M_4\}$ closed loops. Preferential Mo substitution for the different Mo/W POM sites is also clearly evident, with the central core significantly more favored for Mo than any of the other POM positions. This is the site of 2e-reduction and is consistent with the more facile reduction of the 5d transition metal Mo versus its 6d congener W.

While SAXS studies confirm the maintenance of the metal-oxo POM framework in solution under defined conditions, determining whether the amino acid ligands remain

coordinated in solution was also of interest at the outset of this study. Circular dichroism experiment ts indicate that the α-amino acid ligands remain associated the POM framework in solution but that they undergo exchange with free α–amino acid molecules. This exchange is fast on the ^{1}H NMR timescale. Amino acid ligand exchange has been definitely demonstrated by the isolation of an analog with glycine ligands following recrystallization from glycine buffer solution of an analog with norleucine ligands. In contrast, the amino acid ligands do not appear to undergo rapid exchange with water or DMSO. In general, concentrated solutions of the hybrid POMs retain their structure in aqueous solution as long as within a defined pH range (POM to proton concentration ratio) on the timescale of days. The stability is greater in the presence of excess α-amino acid. The reduced, but not the oxidized, Nle-analog is also stable in DMSO on this timescale. Generally, the reduced species are more stable than the oxidized. After one week in solution (no excess of amino acid), both the electronic absorption and CD spectra show a significant loss of intensity and the SAXS scattering patterns & R_g values change, indicating decomposition of the POM, the SAXS and electrochemistry suggest that this is decomposition to a smaller POM and not to simple mono-oxanions. The possible mechanism of decomposition may involve water exchange for the amino acid ligands over days. This would disrupt the intramolecular N-H…O hydrogen bonds between the POM backbone and the eight amino acid ligands, which are likely important for stabilizing the hybrid POM structure. In contrast, in the presence of excess amino acid, SAXS shows some evidence of aggregation after one week in some cases, corresponds to the formation of the well-known POM "blackberries" or "vesicles", which is a subject of ongoing investigation.

Finally, despite the accessibility of stable 2e-reduced analogs, this structural family of hybrid POMs is not promising for redox catalysis because the system is not amenable to

reversible interconversions between the oxidized and reduced forms. However, in principle, similar POMs with accessible photo-reduced forms that can be readily cycled between oxidized and reduced states may prove important for efficient photoreduction catalysis because they do not require an additional photosensitizer as co-catalyst. This work highlights the potential of mixed metal hybrid POMs in this regard and reveals the importance of several key structural features in stabilizing the reduced analogs. Clearly useful are neutral zwitterionic amino acids rather than anionic carboxylate ligands, which serve to minimize the overall negative charge of the hybrid POM and thereby facilitate reduction. Also important, is the potential of "closed metal-oxo loops" of Mo centers that are preferentially reduced and can act as electron reservoirs in mixed-metal molybdotungstates. The challenge remains to synthesize hybrid POMs that strike the right balance between these structural features to afford stability to both oxidized and reduced partners but also allow facile interconversion between them.

ASSOCIATED CONTENT

Supporting Information. X-ray crystallographic files in CIF format for **3w**, **4aw**, **4bw**, **4cw,** **7aw** and **7bw** and additional structural, spectroscopic, electrochemical and computational data. This material is available free of charge via the Internet at http://pubs.acs.org

AUTHOR INFORMATION

Corresponding Author

*E-mail: c.boskovic@unimelb.edu.au

Author Contributions

The manuscript was written through contributions of all authors. All authors have given approval to the final version of the manuscript.

ACKNOWLEDGMENTS

We thank Andy Ohlin for helpful discussions; David Tiede and Xiaobing Zuo for providing the SolX program; Hamish Grant and Matthew Field for assistance with the NMR and XPS, respectively, the Australian Research Council for funding, the Spanish MINECO (project CTQ2011-29054-C02-01/BQU), the DGR of the Generalitat de Catalunya (grant no. 2014SGR199) and the XRQTC.

REFERENCES

1. Nagul, E. A., McKelvie, I. D., Worsfold, P., Kolev, S. D. The molybdenum blue reaction for the determination of orthophosphate revisited: Opening the black box. *Anal. Chim. Acta*. **2015**, *890*, 60-82.

2. Kozhevnikov, I. V. *Catalysis by Polyoxometalates*; Wiley: Chichester, England, 2002.

3. Pope, M. T. *Heteropoly and Isopoly Oxometalates*; Springer-Verlag: Berlin, Germany, 1983.

4. Rinfray, C.; Renaudineau, S.; Izzet, G.; Proust, A covalent polyoxomolybdate-based hybrid with remarkable electron reservoir properties. *Chem. Commun*. **2014**, 8575-8577.

5. Lv, H.; Geletii, Y. V.; Zhao, C.; Vickers, J. W.; Zhu, G.; Luo, Z.; Song, J.; Lian, T.; Musaev, D. G.; Hill, C. L. Polyoxometalate water oxidation catalysts and the production

of green fuel. *Chem. Soc. Rev*. **2012**, *41*, 7572-7589.

6. Yamase, T. Photo- and Electrochromism of Polyoxometalates and Related Materials. *Chem. Rev*. **1998**, *98*, 307-326.

7. Streb, C. New trends in polyoxometalate photoredox chemistry: from photosensitisation to water oxidation catalysis. *Dalton Trans*. **2012**, *41*, 1651-1659.

8. Bernardini, G.; Wedd, A. G.; Zhao, C.; Bond, A. M. Photochemical oxidation of water and reduction of polyoxometalate anions at interfaces of water with ionic liquids or diethylether. *Proc. Natl. Acad. Sci*. **2012**, *109*, 11552-11557.

9. Kogan, V.; Aizenshtat, Z.; Neumann, R. Polyoxometalates as reduction catalysts: Deoxygenation and hydrogenation of carbonyl compounds. *Angew. Chem. Int. Ed.* **1999**, *38*, 3331-3334.

10. von Allmen, K.; Moré, R.; Müller, R.; Soriano-López, J.; Linden, A.; Patzke, G. R. Nickel-Containing Keggin-Type Polyoxometalates as Hydrogen Evolution Catalysts: Photochemical Structure-Activity Relationships. *Chempluschem* **2015**, *80*, 1389-1398.

11. Troupis, A.; Hiskia, A.; Papaconstantinou, E. Synthesis of metal nanoparticles by using polyoxometalates as photocatalysts and stabilizers. **2002**, *41*, 1911-1914.

12. Wang, Y.; Neyman, A.; Arkhangelsky, E.; Gitis, V.; Meshi, L.; Weinstock, I. Self-assembly and structure of directly imaged inorganic-anion monolayers on a gold nanoparticle. *J. Am. Chem. Soc.* **2009**, *131*, 17412-17422.

13. Mitchell, S. G.; de la Fuente, J. M. The synergistic behavior of polyoxometalates and

metal nanoparticles: from synthetic approaches to functional nanohybrid materials. *J. Mater. Chem.* **2012**, *22*, 18091-18100.

14. Poblet, J. M.; López, X.; Bo, C. *Ab initio* and DFT modelling of complex materials: towards the understanding of electronic and magnetic properties of polyoxometalates. *Chem. Soc. Rev.* **2003**, *32*, 297-308.

15. López, X.; Carbó, J. J.; Bo, C.; Poblet, J. M. Structure, properties and reactivity of polyoxometalates: a theoretical perspective. *Chem. Soc. Rev.* **2012**, *41*, 7537-7571.

16. Sadakane, M.; Steckhan, E. Electrochemical Properties of Polyoxometalates as Electrocatalysts. *Chem. Rev*. **1998**, *98*, 219-238.

17. Eda, K.; Osakai, T. How Can Multielectron Transfer Be Realized? A Case Study with Keggin-Type Polyoxometalates in Acetonitrile. *Inorg. Chem.* **2015**, *54*, 2793-2801.

18. Aparicio, P. A.; Poblet, J. M.; López, X. Tungsten redox waves in $[XMW_{11}O_{40}]^{n-}$ (X = P, Si, Al and M = W, Mo, V, Nb, Ti) Keggin compounds - Effect of localised/delocalised charges. *Eur. J. Inorg. Chem.* **2013**, 1910-1916.

19. Müller, A.; Krickemeyer, E.; Meyer, J.; Bögge, H.; Peters, F.; Plass, W.; Diemann, E.; Dillinger, S.; Nonnenbruch, F.; Randerath, M.; Menke, C. $[Mo_{154}(NO)_{14}O_{420}(OH)_{28}(H_2O)_{70}]^{(25\pm5)-}$: A Water-Soluble Big Wheel with More than 700 Atoms and a Relative Molecular Mass of About 24000. *Angew. Chem. Int. Ed. Engl.* **1995**, *34*, 2122-2124.

20. Müller, A; Serain, C. Soluble Molybdenum Blues. *Acc. Chem. Res*. **2000**; *33*, 2-10.

21. Müller, A.; Das, S. K.; Krickemeyer, E.; Kuhlmann, C. Polyoxomolybdate Clusters: Giant Wheels and Balls. *Inorg. Synth*. **2004**, *34*, 191-200.

22. Baker, L. C. W.; Glick, D. C. Present General Status of Understanding of Heteropoly Electrolytes and a Tracing of Some Major Highlights in the History of Their Elucidation. *Chem. Rev.* **1998**, *98*, 3-50

23. Varga Jr, G. M. Heteropoly blues. IV. Spectroscopic and magnetic properties of some reduced polytungstates. *Inorg. Chem.* **1970**, *2003*, 662-667.

24. Prados, R. A.; Pope, M. T. Low-temperature electron spin resonance spectra of heteropoly blues derived from some 1:12 and 2:18 molybdates and tungstates. *Inorg. Chem.* **1976**, *15*, 2547-2553.

25. Kozik, M.; Hammer, C. F.; Baker, L. C. W. Direct Determination by ^{183}W NMR of the Locations of Added Electrons in ESR-Silent Heteropoly Blues. Chemical Shifts and Relaxation Times in Polysite Mixed-Valence Transition-Metal Species. *Chem. Commun.* **1986**, 2748-2749.

26. Kozik, M.; Casan-Pastor, N.; Hammer, C. F.; Baker, L. C. W. Ring Currents in Wholly Inorganic Heteropoly Blue Complexes . Evaluation by a Modification of Evans's Susceptibility Method. *J. Am. Chem. Soc.* **1988**, 7697-7701.

27. Dolbecq, A.; Dumas, E.; Mayer, C. R.; Mialane, P. Hybrid organic-inorganic polyoxometalate compounds: from structural diversity to applications. *Chem. Rev.* **2010**, *110*, 6009-6048.

28. Proust, A.; Matt, B.; Villanneau, R.; Guillemot, G.; Gouzerh, P.; Izzet, Functionalization and post-functionalization: a step towards polyoxometalate-based materials. *Chem. Soc. Rev.* **2012**, *41*, 7605-7622.

29. Long, D.-L.; Tsunashima, R.; Cronin, L. Polyoxometalates: building blocks for functional nanoscale systems. *Angew. Chem. Int. Ed. Engl.* **2010**, *49*, 1736-1758.

30. Santoni, M.-P.; Hanan, G. S.; Hasenknopf, B. Covalent multi-component systems of polyoxometalates and metal complexes: Toward multi-functional organic–inorganic hybrids in molecular and material sciences. *Coord. Chem. Rev.* **2014**, *281*, 64-85.

31. Bassil, B. S.; Kortz, U. *Z.* Recent Advances in Lanthanide-Containing Polyoxotungstates. *Z. Anorg. Allg. Chem.* **2010**, *636*, 2222–2231.

32. Vonci, M.; Boskovic, C. Polyoxometalate-Supported Lanthanoid Single-Molecule Magnets. *Aust. J. Chem.* **2014**, *67*, 1542-1552.

33. Reinoso, S. Heterometallic 3d-4f polyoxometalates: still an incipient field. *Dalton Trans*. **2011**, *40*, 6610-6615.

34. Ma, X.; Yang, W.; Chen, L.; Zhao, J. Significant developments in rare-earth-containing polyoxometalate chemistry: synthetic strategies, structural diversities and correlative properties. *CrystEngComm* **2015**, *17*, 8175-8197.

35. Miras, H. N.; Stone, D. J.; McInnes, E. J. L.; Raptis, R. G.; Baran, P.; Chilas, G. I.; Sigalas, M. P.; Kabanos, T. A; Cronin, L. Solution identification and solid state characterisation of a heterometallic polyoxometalate $\{Mo_{11}V_7\}$: $[Mo^{VI}_{11}V^{V}_{5}V^{IV}_{2}O_{52}(\mu_9$-

$SO_3)]^{7-}$. *Chem. Commun.* **2008**, *52*, 4703-4705.

36. Maksimovskaya, R. I. Nmr Structural Aspects of the Chemistry. *J Struct Chem*. **2006**, *47*, 952-978.

37. Jackson, M. N.; Kamunde-Devonish, M. K.; Hammann, B. A.; Wills, L. A.; Fullmer, L. B.; Hayes, S. E.; Cheong, P. H.-Y.; Casey, W. H.; Nyman, M.; Johnson, D. W. An overview of selected current approaches to the characterization of aqueous inorganic clusters. *Dalton Trans.* **2015**, *44*, 16982-17006.

38. Miras, H. N; Cronin, L. Electrospray and Cryospray Mass Spectrometry: From Serendipity to Designed Synthesis of Supramolecular Coordination and Polyoxometalate Clusters. In: *New Strategies in Chemical Synthesis and Catalysis*. 2012, pp 3-32.

39. Pigga, J. M.; Kistler, M. L.; Shew, C. Y.; Antonio, M. R.; Liu, T. Counterion distribution around hydrophilic molecular macroanions: The source of the attractive force in self-assembly. *Angew. Chem. Int. Ed.* **2009**, *48*, 6538-6542.

40. Kojima, T.; Antonio, M. R.; Ozeki, T. Solvent-driven association and dissociation of the hydrogen-bonded protonated decavanadates. *J. Am. Chem. Soc.* **2011**, *133*, 7248-7251.

41. Yin, P.; Li, T.; Forgan, R. S.; Lydon, C.; Zuo, X.; Zheng, Z. N.; Lee, B.; Long, D.; Cronin, L.; Liu, T. Exploring the programmable assembly of a polyoxometalate-organic hybrid via metal ion coordination. *J. Am. Chem. Soc.* **2013**, *135*, 13425-13432.

42. Goberna-Ferrón, S.; Soriano-López, J.; Galán-Mascarós, J. R.; Nyman, M. Solution Speciation and Stability of Cobalt-Polyoxometalate Water Oxidation Catalysts by X-ray

Scattering. *Eur. J. Inorg. Chem.* **2015**, *2015*, 2833-2840.

43. Yin, P.; Li, T.; Forgan, R. S.; Lydon, C.; Zuo, X.; Zheng, Z. N.; Lee, B.; Long, D.; Cronin, L.; Liu, T. X-ray and Neutron Scattering Study of the Formation of Core–Shell-Type Polyoxometalates. *J. Am. Chem. Soc.* **2016**, *138*, 2638-2643.

44. Ritchie, C; Bryant, G. Microwave assisted synthesis of a mono organoimido functionalized Anderson polyoxometalate. *Dalton Trans*. **2015**, *44*, 20826-20829.

45. Antonio, M. R.; Nyman, M.; Anderson, T. M. Direct observation of contact ion-pair formation in aqueous solution. *Angew. Chem. Int. Ed.* **2009**, *48*, 6136-6140.

46. Hasenknopf, B.; Micoine, K.; Lacôte, E.; Thorimbert, S.; Malacria, M.; Thouvenot, R. Chirality in Polyoxometalate Chemistry. *Eur. J. Inorg. Chem.* **2008**, *2008*, 5001-5013.

47. Du, D.-Y.; Yan, L.-K.; Su, Z.-M.; Li, S.-L.; Lan, Y.-Q.; Wang, E.-B. Chiral polyoxometalate-based materials: From design syntheses to functional applications. *Coord. Chem. Rev.* **2013**, *257*, 702-717.

48. Liu, D.; Tan, H.-Q.; Chen, W.-L.; Li, Y.-G.; Wang, E.-B. Resolution of chiral polyoxoanion $[P_2Mo_{18}O_{62}]^{6-}$ with histidine. *CrystEngComm* **2010**, *12*, 2044-2046.

49. Wang, Y.; Shi, L.; Yang, Y.; Li, B.; Wu, L. Induced circular dichroism of polyoxometalates via electrostatic encapsulation with chiral organic cations. *Dalton Trans.* **2014**, *43*, 13178-13186.

50. Wang, Y.; Li, H.; Wu, C.; Yang, Y.; Shi, L.; Wu, L. Chiral heteropoly blues and controllable switching of achiral polyoxometalate clusters. *Angew. Chem. Int. Ed. Engl.*

2013, *52*, 4577-4581.

51. Kortz, U.; Savelieff, M. G.; Ghali, F. Y. A.; Khalil, L. M.; Maalouf, S. A.; Sinno, D. I. Heteropolymolybdates of As. *Angew. Chem. Int. Ed. Engl.* **2002**, 4070-4073.

52. Naruke, H.; Iijima, J.; Sanji, T. Enantioselective Resolutions and Circular Dichroism Studies Polyoxometalates. *Inorg. Chem.* **2011**, 7535-7539.

53. Fang, X.; Anderson, T. M.; Hill, C. L. Enantiomerically pure polytungstates: Chirality transfer through zirconium coordination centers to nanosized inorganic clusters. *Angew. Chemie Int. Ed.* **2005**, *44*, 3540-3544.

54. Ju, W.-W.; Zhang, H.-T.; Xu, X.; Zhang, Y.; Xu, Y. Enantiomerically pure lanthanide-organic polytungstates exhibiting two-photon absorption properties. *Inorg. Chem.* **2014**, *53*, 3269-3271.

55. Vonci, M.; Akhlaghi Bagherjeri, F.; Hall, P. D.; Gable, R. W.; Zavras, A.; O'Hair, R. a. J.; Liu, Y.; Zhang, J.; Field, M. R.; Taylor, M. B.; Du Plessis, J.; Bryant, G.; Riley, M.; Sorace, L.; Aparicio, P. A.; López, X.; Poblet, J. M.; Ritchie, C.; Boskovic, Modular Molecules: Site-Selective Metal Substitution, Photoreduction, and Chirality in Polyoxometalate Hybrids. *Chem. Eur. J.* **2014**, *20*, 14102-14111.

56. Leyrie, M.; Martin-Frère, J.; Hervé, G. Obtention et propiétés de quelques tungstoarséniates(III)*C. R. Acad. Sci., Ser. II **1974**, 279,* 895.

57. Wassermann, K.; Pope, M. T. Large Cluster Formation through Multiple Substitution with Lanthanide Cations. *Inorg. Chem* **2001**, *40*, 2763-2768.

58. Chen, W.; Li, Y.; Wang, Y.; Wang, E.; Su, Z. Building block approach to nanostructures: step-by-step assembly of large lanthanide-containing polytungstoarsenate aggregates. *Dalton Trans.* **2007**, 4293-4301.

59. Feng, X.-J.; Han, H.-Y.; Wang, Y.-H.; Li, L.-L.; Li, Y.-G.; Wang, E.-B. Assembly of chainlike polyoxometalate-based lanthanide complexes in one-pot reaction system. *CrystEngComm* **2013**, *15*, 7267-7273.

60. Kortz, U.; Savelieff, M. G.; Bassil, B. S.; Dickman, M. H. A Large, Novel Polyoxotungstate: $[As^{III}_6W_{65}O_{217}(H_2O)_7]^{26-}$. *Angew. Chem. Int. Ed. Engl.* **2001**, *40*, 3384-3386.

61. Dolomanov, O. V.; Bourhis L. J.; Gildea, R. J.; Howard, J. A. K.; Puschmann, H. OLEX2: A complete structure solution, refinement and analysis program. *J. Appl. Cryst*. **2009**, *42*, 339-341.

62. Sheldrick, G. M. SHELXT – Integrated space-group and crystal-structure determination. *Acta Cryst.* **2015**, *A71*, 3-8.

63. Sheldrick, G. M. Crystal structure refinement with SHELXL. *Acta Cryst* **2015**, *C71*, 3-8.

64. Spek, A. L. Structure validation in chemical crystallography. *Acta Cryst.* **2009**, *D65*, 148-155.

65. Zuo, X.; Cui, G.; Merz, K. M.; Zhang, L.; Lewis, F. D.; Tiede, D. M. X-ray diffraction "fingerprinting" of DNA structure in solution for quantitative evaluation of molecular dynamics simulation. *Proc. Natl. Acad. Sci.* **2006**, *103*, 3534-3539.

66. O'Donnell, J. L.; Zuo, X.; Goshe, A. J.; Sarkisov, L.; Snurr, R. Q.; Hupp, J. T.; Tiede, D. M. Solution-phase structural characterization of supramolecular assemblies by molecular diffraction. *J. Am. Chem. Soc.* **2007**, *129*, 1578-1585.

67. Moore, P. B. Small-angle Scattering. Information Content and Error Analysis. *J. Appl. Cryst*. **1980**, *7*, 168-175.

68. Gottlieb, H. E.; Kotlyar, V.; Nudelman, A. NMR Chemical Shifts of Common Laboratory Solvents as Trace Impurities. *J. Org. Chem.* **1997**, *3263*, 7512-7515.

69. (a) ADF2013.01, SCM, Theoretical Chemistry, Vrije Universiteit, Amsterdam, The Netherlands, http://www.scm.com. (b) Fonseca Guerra, C.; Snijders, J. G.; te Velde, G.; Baerends, E. J. Towards an order-N DFT method. *Theor. Chem. Acc.* **1998**, *99*, 391. (c) te Velde, G.; Bickelhaupt, F. M.; Baerends, E. J.; Guerra, C. F.; van Gisbergen, S. J. A.; Snijders, J. G.; Ziegler, T. Chemistry with ADF. *J. Comput. Chem.* **2001**, *22*, 931.

70. (a) Becke, A. D. Density functional calculations of molecular bond energies. *J. Chem. Phys.* **1986**, *84*, 4524. (b) Becke, A. D. Density-functional exchange-energy approximation with correct asymptotic behavior. *Phys. Rev.* **1988**, *A38*, 3098. (c) Vosko, S. H.; Wilk, L.; Nusair, M. Accurate spin-dependent electron liquid correlation energies for local spin density calculations: a critical analysis. *Can. J. Phys.* **1980**, *58*, 1200. (d) Perdew, J. P. *Phys. Rev.* **1986**, *B33*, 8822. (e) Perdew, Density-functional approximation for the correlation energy of the inhomogeneous electron gas. J. P. *Phys. Rev.* **1986**, *B34*, 7406.

71. (a) Klamt, A.; Schüürmann, G. COSMO: a new approach to dielectric screening in

solvents with explicit expressions for the screening energy and its gradient. *J. Chem. Soc, Perkin Trans*. **1993**, *2*, 799. (b) Andzelm, J.; Kölmel, C.; Klamt, A. Incorporation of solvent effects into density functional calculations of molecular energies and geometries. *J. Chem. Phys*. **1995**, *103*, 9312. (c) Klamt, A. Conductor-like Screening Model for Real Solvents: A New Approach to the Quantitative Calculation of Solvation Phenomena. *J. Phys*. *Chem.* **1995**, *99*, 2224. (d) Pye, C. C.; Ziegler, T. An implementation of the conductor-like screening model of solvation within the Amsterdam density functional package. *Theor. Chem. Acc*. **1999**, *101*, 396.

72. Brown, I. D. *The Chemical Bond in Inorganic Chemistry: The Bond Valence Model*, Oxford University Press, 2002.

73. Brown, I. D. Altermatt, D. Bond-Valence Parameters Obtained from a Systematic Analysis of the Inorganic Crystal Structure Database. *Acta Cryst.* **1985**, *B41*, 244-247.

74. Vonci, M.; Boskovic, C. unpublished results.

75. Thouvenot, R.; Fournier, M.; Franck, R.; Rocchiccioli-Deltcheff, C. Vibrational investigations of polyoxometalates. 3. Isomerism in molybdenum(VI) and tungsten(VI) compounds related to the Keggin structure. *Inorg. Chem.* **1984**, *23*, 598-605.

76. Way, D. M.; Cooper, J. B.; Sadek, M.; Vu, T.; Mahon, P. J.; Bond, A. M.; Brownlee, R. T. C.; Wedd, A. G. Systematic Electrochemical Synthesis of Reduced Forms of the alpha-$[S_2Mo_{18}O_{62}]^{4-}$ Anion. *Inorg. Chem.* **1998**, *37*, 604-613.

77. Garvey, J. F.; Pope, M. T. Chirality of oxidized and reduced octadecamolybdodiphosphate anions. Observation of a Pfeiffer effect. *Inorg. Chem.* **1978**, *17*, 1115–1118.

78. Sun, H.-R.; Zhang, S.-Y.; Xu, J.-Q.; Yang, G.-Y.; Shi, T.-S. *J.* Electrochemical and in-situ UV-visible-near-IR and FTIR spectroelectrochemical characterisation of the mixed-valence heteropolyanion $PMo_{12}O_{40}^{n-}$ (n = 4, 5, 6, 7) in aprotic media. *J. Electroanal. Chem.* **1998**, *455*, 57-68.

79. Fournier, M.; Rocchiccioli-Deltcheff, C.; Kazansky, L. P. Infrared spectroscopic evidence of bipolaron delocalization in reduced heterododecamolybdates. *Chem. Phys. Lett.* **1994**, *223*, 297-300.

80. Bond, A. M.; Boskovic, C.; Sadek, M.; Brownlee, R. T. C. Electrosynthesis and solution structure of six-electron reduced forms of metatungstate, $[H_2W_{12}O_{40}]^{6-}$. *J. Chem. Soc. Dalton Trans.* **2001**, 187-196.

81. Fleisch, T. H. An XPS study of the UV reduction and photochromism of MoO_3 and WO_3. *J. Chem. Phys.* **1982**, *76*, 780-786.

82. Feng, W.; Ding, Y.; Liu, Y.; Lu, R. The photochromic process of polyoxometalate-based nanocomposite thin film by in situ AFM and spectroscopy. *Mater. Chem. Phys.* **2006**, *98*, 347-352.

83. Wang, L.; Yin, P.; Zhang, J.; Hao, J.; Lv, C.; Xiao, F.; Wei, Y. X-octamolybdate $[Mo^{V}_4Mo^{VI}_4O_{24}]^{4-}$: An unusual small polyoxometalate in partially reduced form from nonaqueous solvent reduction. *Chem. Eur. J.* **2011**, *17*, 4796-4801.

84. Zhang, J.; Li, W.; Wu, C.; Li, B.; Zhang, J.; Wu, L. Redox-controlled helical self-assembly of a polyoxometalate complex. *Chem. Eur. J.* **2013**, *19*, 8129-8135.

85. Sanchez, C.; Livage, J.; Launay, J. P.; Fournier, M.; Jeannin, Y. Electron Delocalization in Mixed-Valence Molybdenum. *J. Am. Chem. Soc* **1982**, *104*, 3194-3202.

86. Sanchez, C.; Livage, J.; Launay, J. P.; Fournier, M. Electron Delocalization in Mixed-Valence Tungsten. *J. Am. Chem. Soc* **1983**, 6817-6823.

87. Duncan, D. C.; Hill, C. L. Synthesis and Characterization of the Mixed-Valence Diamagnetic Two-Electron-Reduced Isopolytungstate $[W_{10}O_{32}]^{6-}$. Evidence for an Asymmetric d-Electron Distribution over the Tungsten Sites. *Inorg. Chem.* **1996**, *35*, 5828-5835.

88. Yin, P.; Li, D.; Liu, T. Solution behaviors and self-assembly of polyoxometalates as models of macroions and amphiphilic polyoxometalate-organic hybrids as novel surfactants. *Chem. Soc. Rev.* **2012**, *41*, 7368-7383.

89. Knoppe, S.; Dharmaratne, A. C.; Schreiner, E.; Dass, A.; Bürgi, T. Ligand Exchange Reactions on Au_{38} and Au_{40} Clusters : A Combined Circular Dichroism and Mass Spectrometry Study. *J. Am. Chem. Soc.* **2010**, *132*, 16783-16789.

90. Amdursky, N.; Stevens, M. M. Circular Dichroism of Amino Acids: Following the Structural Formation of Phenylalanine. *ChemPhysChem* **2015**, *16*, 2768-2774.

91. Schäffer, C.; Merca, A.; Bögge, H.; Todea, A. M.; Kistler, M. L.; Liu, T.; Thouvenot, R.; Gouzerh, P.; Müller, A. Unprecedented and differently applicable pentagonal units in a dynamic library: a keplerate of the type $\{(W)W_5\}_{12}\{Mo_2\}_{30}$. *Angew. Chem. Int. Ed. Engl.* **2009**, *48*, 149-153.

92. Grego, A.; Müller, A.; Weinstock, I. A. Stepwise-resolved thermodynamics of hydrophobic self-assembly. *Angew. Chem. Int. Ed. Engl.* **2013**, *52,* 8358-8362.

93. Müller, A.; Gouzerh, P. Capsules with highly active pores and interiors: versatile platforms at the nanoscale. *Chem. Eur. J.* **2014**, *20*, 4862-4873.

94. Doddrell, D.; Allerhand, A. Segmental motion in liquid 1-decanol. Application of natural-abundance carbon-13 partially relaxed Fourier transform nuclear magnetic resonance. *J. Am. Chem. Soc.* **1971**, *159*, 1558-1559.

95. Jardetzky, O. NMR studies of macromolecular dynamics. *Acc. Chem. Res*. **1981**, *14*, 291-298.

96. Lin, S.; Hong, T.; Tung, J.; Chen, J. Molecular Structures of Ge(tpp)$(OAc)_2$ and In(tpp)(OAc) and Their Implications : Correlations between the ^{13}C NMR Chemical Shift of the Acetato Ligand and Different Types of Carboxylate Coordination in M(por)$(OAc)_n$ {por = tpp (5,10,15,20-Tetraphenylporphyrinate), tmpp (5,10,15,20-Tetrakis(4-methoxyphenyl)porphyrinate), tpyp (5,10,15,20-Tetrakis(4-pyridyl)porphyrinate); M = Ga, In, Tl, Ge, Sn; n = 1, 2}. *Inorg. Chem.* **1997**, *1669*, 3886-3891.

97. Ye, B. H.; Li, X. Y.; Williams, I. D.; Chen, X. M. Synthesis and structural characterization of di- and tetranuclear zinc complexes with phenolate and carboxylate bridges. Correlations between ^{13}C NMR chemical shifts and carboxylate binding modes. *Inorg. Chem.* **2002**, *41*, 6426-6431.

98. Yan, L.; López, X.; Carbó, J. J.; Sniatynsky, R.; Duncan, D. C.; Poblet, J. M. On the origin of alternating bond distortions and the emergence of chirality in polyoxometalate

anions. *J. Am. Chem. Soc.* **2008**, *130*, 8223-8233.

99. López, X.; Bo, C.; Poblet, J. M. Electronic Properties of Polyoxometalates : Electron and Proton Affinity of Mixed-Addenda Keggin and Wells - Dawson Anions. *J. Am. Chem. Soc.* **2002**, *124*, 12574-12582.

100. Parent, L.; Aparicio, P. A.; De Oliveira, P.; Teillout, A. L.; Poblet, J. M.; López, X.; Mbomekallé, I. M. Effect of electron (De)localization and pairing in the electrochemistry of polyoxometalates: Study of Wells-Dawson molybdotungstophosphate derivatives. *Inorg. Chem.* **2014**, *53*, 5941-5949.

101. López, X.; Fernández, J. A.; Poblet, J. M. Redox properties of polyoxometalates: new insights on the anion charge effect. *Dalton Trans.* **2006**, 1162-1167.

Table of Contents Entry

An experimental and computational investigation of a family of heterometallic polyoxometalates with amino acid ligands reveals a robust polyoxometalate framework that is readily modified in terms of the nuclearity of the metal-oxo core, the metal composition, the redox state and the amino acid ligands.